arXiv:2607.28752v2 [cond-mat.mtrl-sci] 11 Nov 2026

Local B-site chemistry controls oxygen-vacancy energetics in Ca–Ce–Ti–Mn perovskites for thermochemical hydrogen production†

Manish Kumar,‡[a] Natalia Ali,‡[b] Matthew D. Witman,[c] Shang Zhai,[d,e] James E. Miller,[f] Ivan Ermanoski,[f] Ellen B. Stechel,[g] and Robert B. Wexler*[a]

Two-step thermochemical water splitting driven by concentrated solar heat offers a scalable route to renewable hydrogen, but practical deployment requires oxide materials whose oxygen-vacancy formation energies balance facile reduction with favorable reoxidation. Perovskite solid solutions provide compositional flexibility to tune this balance, yet the relationship between bulk stoichiometry and local defect energetics remains poorly understood. Here we map oxygen-vacancy formation energetics across Ca–Ce–Ti–Mn (CCTM) perovskites using first-principles calculations combined with two complementary fitted models. A coverage-constrained special quasirandom structure approach is designed to sample all fifteen symmetry-distinct oxygen nearest-neighbor environments. We develop a crystal-feature model whose fitted coefficients directly encode the underlying Born–Haber thermochemistry, and we fine-tune a defect graph neural network to model potential nonlinear structure–composition–defect coupling beyond the linear form of the crystal-feature model. Local B-site chemistry dominates the oxygen-vacancy formation energy (E_v): varying the nearest-neighbor Mn fraction (B site) shifts E_v by 1.0–1.5 eV depending on local Ce content, whereas A-site Ce variation contributes a smaller, Mn-dependent shift of 0.2–0.6 eV. This hierarchy indicates that short-range B-site cation order, if it can be established and kinetically retained through targeted processing, is a candidate means of tuning redox performance without changing bulk composition. Composition-space maps show a Ce/Mn-balanced region (approximately 29–33 % Ce on the A site and 58–67 % Mn on the B site) that combines a high fraction of vacancy sites within the targeted E_v window with phase stability and solubility, where the predicted redox cycle capacity $\Delta\delta$ is comparable to or exceeds the ceria benchmark at substantially lower reduction temperatures ($T_{red} = 1350\,^{\circ}$C vs. $\sim$1600 °C for ceria). Experimental measurements on three CCTM compositions show $\Delta\delta$ increasing monotonically with Ce content under cycling protocols close to the model conditions, consistent with the qualitative trend from the fitted models. The interpretable framework provides both compositional screening capability and mechanistic design rules expected to transfer to related perovskite families for solar thermochemical hydrogen production.

Introduction

Thermochemical water splitting driven by concentrated solar heat offers a renewable route to hydrogen production that can help decarbonize transportation, manufacturing, and chemical synthesis.[1,2] In the canonical two-step redox cycle, a metal oxide is thermally reduced at high temperature, then reoxidized with steam at a lower temperature to produce hydrogen.[2,3] For the oxides considered here, which accommodate oxygen off-stoichiometry, thermal reduction proceeds by oxygen-vacancy formation. Ceria remains the benchmark material: it exhibits fast kinetics, stable oxygen-exchange capacity over repeated cycling, and a favorable reduction entropy that lowers the temperature at which thermal reduction becomes thermodynamically favorable.[2–5] This favorable reduction entropy is largely electronic in origin: the onsite electronic configurational entropy of reduction is largest for the Ce^{4+}/Ce^{3+} couple among the f elements.[6] In addition, the charged (ionized) nature of ceria's oxygen-vacancy defects underlies its ability to sustain hydrogen production even at high H_2/H_2O ratios, the most demanding reoxidation regime for practical operation, whereas many candidate oxides are limited to far more dilute ratios.[4] However, ceria's high reduction enthalpy requires operating temperatures above 1500 °C, imposing stringent constraints on reactor design and limiting cost competitiveness.[2,4,7–10] Alternative materials that reduce at lower temperatures while maintaining comparable

[a] Department of Chemistry and Institute of Materials Science and Engineering, Washington University in St. Louis, St. Louis, MO 63130, USA. E-mail: wexler@wustl.edu
[b] ASU LightWorks® and the School for Engineering of Matter, Transport and Energy, Arizona State University, Tempe, AZ 85287-8204, USA.
[c] Sandia National Laboratories, Livermore, CA 94550, USA.
[d] Department of Mechanical and Aerospace Engineering, The Ohio State University, Columbus, OH 43210, USA.
[e] School of Earth Sciences, The Ohio State University, Columbus, OH 43210, USA.
[f] ASU LightWorks® and the School of Sustainability, Arizona State University, Tempe, AZ 85287-8204, USA.
[g] ASU LightWorks® and the School of Molecular Sciences, Arizona State University, Tempe, AZ 85287-8204, USA.
‡ These authors contributed equally to this work.
† Electronic Supplementary Information (ESI) available: magnetic moments and oxidation-state assignments; density of states and metallic character; crystal-feature-model parity; the vacancy–vacancy electrostatic upper bound; powder X-ray diffraction; thermogravimetric analysis; the finite-temperature thermodynamic formalism with a worked example; the defect graph neural network model; configurational sensitivity of bulk energetics under SQS sampling; Brillouin-zone sampling convergence; and the atomic-property values used in the crystal-feature-model descriptors.

hydrogen yields are therefore essential for practical deployment.[11]

Perovskite oxides ($ABO_{3-\delta}$) have emerged as promising alternatives because their compositional flexibility enables systematic tuning of vacancy formation energetics.[1,2,12] McDaniel et al. introduced the $LaAlO_3$-derived series $(Sr_xLa_{1-x})(Mn_yAl_{1-y})O_{3-\delta}$ (SLMA), in which Sr^{2+} substitution on the A site introduces charge imbalance that promotes vacancy formation, while Mn on the B site provides multivalent redox centers ($Mn^{4+}/Mn^{3+}/Mn^{2+}$) for reversible oxygen exchange.[13] Subsequent work expanded this design space through A-site entropy engineering,[14] size-mismatch and disorder effects,[15] and B-site substitution with Cr, Co, Ni, Fe, or Ga.[16–24] Complementary processing innovations, including foamed morphologies, have improved heat and mass transport.[25]

A complementary design strategy uses mixed Ce–Mn B-site occupancy in $BaCe_xMn_{1-x}O_{3-\delta}$ (BCM).[26] The large Ba^{2+} cation stabilizes a lattice that tolerates significant oxygen off-stoichiometry, while the vacancy formation energy, set jointly by the Ce^{4+}/Ce^{3+} and Mn^{4+}/Mn^{3+} redox couples, falls within the range required for efficient cycling. The $Ba(Ce_{0.25}Mn_{0.75})O_{3-\delta}$ composition reduces below 1400 °C with fast kinetics, and Barcellos et al. report approximately three times the hydrogen yield of ceria when both are reduced at 1350 °C, a temperature below ceria's favorable reduction window.[26,27] More recently, Perry et al. combined machine learning with density functional theory (DFT) to design $Ba_{0.875}Ca_{0.125}Zr_{0.875}Mn_{0.125}O_{3-\delta}$, predicted by thermodynamic system-model simulations to reduce at a maximum temperature of 1523 °C versus 1734 °C for ceria.[28]

Among these materials, Ca–Ce–Ti–Mn (CCTM) perovskites have been identified as promising candidates. Initial DFT calculations predicted favorable vacancy energetics with redox activity on both Ce and Mn,[29] and subsequent work demonstrated that Ti substitution enhances phase stability while placing vacancy formation energies near the target 3.4–3.9 eV range established in our earlier thermodynamic analysis.[2,30] Experimental studies on the reference composition $Ca_{2/3}Ce_{1/3}Ti_{1/3}Mn_{2/3}O_3$ (CCTM2112) confirmed hydrogen productivities of $\sim$10 mmol H_2/mol atom CCTM2112 per cycle at 1350 °C, with rapid and reversible kinetics.[30] Ce reduction on the A site, in addition to conventional B-site Mn reduction, was identified as a contributor to the redox activity, providing a design variable absent in B-site-only Ce perovskites such as BCM.[30]

Despite this progress, the relationship between bulk stoichiometry and local defect energetics in CCTM perovskites remains poorly understood, limiting rational optimization. Prior computational studies examined single compositions using representative supercells that do not systematically sample the diversity of local oxygen environments present in disordered solid solutions.[29,30] Complementary high-throughput first-principles screening has mapped oxygen-vacancy formation energies and phase stability across large perovskite and oxide sets, generally without resolving the distribution of distinct local oxygen environments within a disordered composition.[31–33] Furthermore, although machine-learning models have been applied to screen perovskite compositions,[34–36] many of these models lack physical transparency, obscuring the factors that control vacancy formation. A predictive framework connecting local cation chemistry to macroscopic redox performance through interpretable descriptors would enable both rational composition optimization and transferable design rules for related perovskite families.

The principal advance of this work is the systematic resolution of all fifteen symmetry-distinct oxygen nearest-neighbor environments in the CCTM solid solution and the demonstration that local B-site chemistry, rather than bulk stoichiometry, dominates oxygen-vacancy energetics; the composition-space screening that follows is an application of this framework rather than its central result. To establish this, we combine first-principles defect thermochemistry with two complementary fitted models to map oxygen-vacancy energetics across the CCTM composition space. To ensure complete sampling of local chemical diversity, we introduce a coverage-constrained special quasirandom structure (SQS) methodology in which each supercell realizes all fifteen symmetry-distinct oxygen nearest-neighbor environments. We develop an interpretable crystal-feature model (CFM) whose fitted coefficients directly encode the underlying Born–Haber thermochemistry, and we benchmark these predictions against a retrained defect graph neural network (dGNN).

This analysis shows that local B-site chemistry dominates vacancy energetics: varying the Mn fraction among nearest-neighbor B sites shifts E_v by 1.0–1.5 eV depending on local Ce content, whereas A-site Ce variation contributes a smaller, Mn-dependent shift of 0.2–0.6 eV; this hierarchy indicates that short-range B-site cation order, if it can be kinetically retained, is a candidate means of tuning redox performance without changing bulk composition. Combining the in-window E_v fraction with phase stability, we identify $Ca_{0.67}Ce_{0.33}Ti_{0.33}Mn_{0.67}O_3$ (CCTM2112) and $Ca_{0.71}Ce_{0.29}Ti_{0.42}Mn_{0.58}O_3$ as the most promising candidates among the six compositions examined (Table 1), with predicted cycle capacities comparable to or exceeding ceria at substantially lower reduction temperatures; experimental measurements on three compositions are consistent with these predictions. The interpretable framework provides both compositional screening capability and mechanistic design rules expected to transfer to related perovskite families.

Results

Compositional design space

Maximizing hydrogen yield in thermochemical water splitting requires oxygen-vacancy formation energies, E_v, that are low enough to permit thermal reduction yet high enough to drive steam reoxidation, together with a phase-stable host that withstands repeated cycling. Guided by the favorable hydrogen productivity of CCTM2112 ($\sim$10 mmol H_2/mol atom CCTM2112 per cycle at 1350 °C; reduction and reoxidation conditions comparable to those in Table 3),[30] we examined six Ca–Ce–Ti–Mn perovskites (host structure in Fig. 1a; local oxygen coordination in Fig. 1b) in which only the A-site Ce fraction and B-site Mn fraction vary, with Ca retained as the majority A-site cation (Table 1). The Ce mole fraction X_{Ce} spans 0.25–0.37, bracketing the empirically observed solubility limit ($\sim 1/3$) above which CeO_2 segregation is expected.[30,37,38] Four compositions lie along the line $X_{Mn} = 2X_{Ce}$ (Fig. 1c); this relation enforces nominal charge compensation between Ce and Mn (each Ce^{4+} substituting for Ca^{2+} on the A site is balanced by

two Mn^{3+} substituting for Ti^{4+} on the B site) and enables a test of whether maintaining this balance promotes reversible oxygen exchange. Two additional compositions hold $X_{Ce} = 1/3$ while deviating from the 2:1 line toward Mn-poor ($X_{Mn} = 0.58$) and Mn-rich ($X_{Mn} = 0.75$) limits, decoupling A-site and B-site effects. Together, these six compositions enable a systematic assessment of how bulk stoichiometry shapes both thermodynamic stability (E_{hull}) and the distribution of local vacancy formation energies.

Phase stability and vacancy energetics

Phase stability under repeated redox cycling is essential for practical thermochemical hydrogen production. We assess intrinsic stability using the zero-kelvin energy above the convex hull, E_{hull}, for each composition (Table 1). All six values lie within 18–39 meV atom^{-1}, comparable to the metastability range typical of experimentally observed complex oxides;[39] CCTM2112, in the upper portion of this range at 33 meV atom^{-1}, has been synthesized in prior work.[30] Along the charge-compensation line $X_{Mn} = 2X_{Ce}$ (Fig. 2, blue circles), E_{hull} increases monotonically with X_{Ce}, consistent with progressive deviation from the stable $CaTiO_3$ end member. At fixed $X_{Ce} = 1/3$ (Fig. 2, red squares), increasing X_{Mn} from 0.58 to 0.75 raises E_{hull} more modestly (31–35 meV atom^{-1}), indicating that B-site variation alone is less destabilizing than simultaneous A- and B-site changes.

Having established that all six compositions are thermodynamically accessible, we next assess their oxygen-exchange activity through the formation energy of a neutral oxygen vacancy, E_v. In these metallic hosts (ESI Fig. S2), the neutral vacancy is the relevant charge state (see Methods). E_v accounts for both the cost of removing a neutral oxygen atom to form $ABO_{3-\delta}$ and the stabilization gained when the two electrons left on the lattice are accommodated by reducible neighboring cations (equivalently, O^{2-} departs as $\frac{1}{2}O_2$, leaving its two electrons behind). Reducible couples such as Mn^{4+}/Mn^{3+} lower E_v by providing favorable electron-accepting states, whereas the less reducible Ti^{4+}/Ti^{3+} raises it; the role of Ce is intermediate and composition-dependent, as discussed below.

Distributions centered in the 3.4–3.9 eV range are expected to balance high-temperature reduction with steam reoxidation: the upper bound of the window reflects the requirement that E_v be low enough for thermal reduction to be accessible, and the lower bound that it remain high enough to retain a thermodynamic driving force for steam reoxidation, the same competition formalized at finite temperature through the reduction and water-splitting oxygen chemical potentials (eqn (6) and (8) in Methods).[2] This 0 K E_v target window is distinct from the explicit finite-temperature cycle-capacity evaluation, which uses the specific T–P_{O_2} values in Methods. All six CCTM compositions populate this target window to varying extents (Table 2 and Fig. 3). Along the charge-compensation series $X_{Mn} = 2X_{Ce}$, the median E_v values cluster tightly between 3.46 and 3.58 eV, and the fraction of sites within the target range peaks at $X_{Ce} = 0.33$, where 49 % of vacancies fall between 3.4 and 3.9 eV. The mean–median difference is at most 0.20 eV across all compositions, indicating only mild skewness.

At fixed $X_{Ce} = 1/3$, varying X_{Mn} shifts both the central tendency and the spread of the distribution (Fig. 3). The median rises from 3.31 eV at $X_{Mn} = 0.58$ to 3.46 eV at $X_{Mn} = 0.67$ (maximizing the in-window fraction at 49 %), then drops to 3.21 eV at $X_{Mn} = 0.75$. In this Mn-rich limit, 87 % of vacancies fall below 3.4 eV, indicating overly facile reduction and a diminished thermodynamic driving force for reoxidation. These trends reflect the competing influences of cation reducibility: higher local Mn content lowers E_v through the favorable Mn^{4+}/Mn^{3+} couple, while Ti raises E_v. An intermediate Mn fraction balances these effects, placing the largest fraction of sites in the desired window. From a materials-selection perspective, $Ca_{0.67}Ce_{0.33}Ti_{0.33}Mn_{0.67}O_3$ (49 % in-window; $E_{hull} = 33$ meV atom^{-1}) and $Ca_{0.71}Ce_{0.29}Ti_{0.42}Mn_{0.58}O_3$ (44 % in-window; $E_{hull} = 26$ meV atom^{-1}) are the candidates that best combine a high in-window fraction with phase stability.

Local cation control of vacancy energetics

To connect local cation chemistry with vacancy energetics, we define a vacancy's local composition (Fig. 1b) in terms of the Ce fraction among its four A-site nearest neighbors (x_{Ce}) and the Mn fraction among its two B-site nearest neighbors (x_{Mn}). Uppercase symbols (X_{Ce}, X_{Mn}) denote bulk-averaged compositions (Table 1), while lowercase symbols denote local values around a specific vacancy site (Fig. 4). Because only two cation types occupy each sublattice, the remaining fractions are fixed by stoichiometry: $x_{Ca} = 1 - x_{Ce}$ and $x_{Ti} = 1 - x_{Mn}$. This mapping assigns each of the fifteen symmetry-distinct vacancy environments in the SQS supercells to a unique (x_{Ce}, x_{Mn}) pair, enabling direct correlation with the local vacancy formation energy E_v.

The B-site chemistry is the primary control on E_v. Increasing x_{Mn} from 0 to 1 lowers E_v by ~1.5 eV in $Ca_{0.71}Ce_{0.29}Ti_{0.42}Mn_{0.58}O_3$ (Fig. 4). The dependence on the local Mn fraction dominates, whereas the dependence on local Ce is weaker and nonmonotonic; varying x_{Ce} shifts E_v by 0.2–0.6 eV depending on local Mn content. The target 3.4–3.9 eV window is thus accessible via two routes: high local Mn content with high Ce, or moderate Mn with low Ce.

These observations motivate a physics-informed linear model of the form

$$E_v = \beta_b \langle E_b \rangle + \beta_r \langle V_r \rangle + \beta_0, \quad (1)$$

where $\langle E_b \rangle$ is the average M–O bond-dissociation energy and $\langle V_r \rangle$ is the average crystal reduction potential (the reduction potential of a cation couple evaluated in the oxide crystal rather than in aqueous solution[34]), both computed over all six nearest-neighbor cations (four A-site, two B-site). The fitted coefficients encode the effective contributions of each term to vacancy formation. Substituting Mn for Ti weakens M–O bonds and provides a more favorable reduction couple (Mn^{4+}/Mn^{3+}), both of which lower E_v; replacing Ca with Ce modifies $\langle V_r \rangle$ more modestly, consistent with the smaller and nonmonotonic influence of A-site composition.

A Huber regression (which down-weights outliers) fitted to 90 vacancy energies from the strongly constrained and appropriately normed functional with Hubbard U corrections (SCAN+U) supports this picture (ESI Fig. S3). The model achieves a mean absolute error of 0.175(15) eV across 1000 random 50 %/50 % train–test splits. This accuracy is comparable to that of earlier linear descriptor models, which predict oxygen-vacancy formation energies in

Table 1 CCTM compositions examined in this work. X_{Ce} and X_{Mn} denote A-site Ce and B-site Mn mole fractions, respectively. E_{hull} is the zero-kelvin energy above the convex hull ($meV\,atom^{-1}$). Calculated oxidation states for Ce and Mn are assignments from SCAN+U local magnetic moments (ESI Section S1), not measurements; the integer labels classify calculated moments, and Ce sites labeled 3 have fractional $4f$ occupation (Ce^{3+}-like).

	Mole fractions				Calculated oxidation states	
CCTM chemical formula	X_{Ce}	X_{Mn}	X_{Ce}/X_{Mn}	E_{hull} ($meV\,atom^{-1}$)	Ce	Mn
$Ca_{0.75}Ce_{0.25}Ti_{0.50}Mn_{0.50}O_3$	0.25	0.50	1/2	18	3	4, 3
$Ca_{0.71}Ce_{0.29}Ti_{0.42}Mn_{0.58}O_3$	0.29	0.58	1/2	26	3	4, 3
$Ca_{0.67}Ce_{0.33}Ti_{0.33}Mn_{0.67}O_3$	0.33	0.67	1/2	33	4, 3	4, 3
$Ca_{0.63}Ce_{0.37}Ti_{0.25}Mn_{0.75}O_3$	0.37	0.75	1/2	39	3	4, 3
$Ca_{0.67}Ce_{0.33}Ti_{0.42}Mn_{0.58}O_3$	0.33	0.58	>1/2	31	3	4, 3
$Ca_{0.67}Ce_{0.33}Ti_{0.25}Mn_{0.75}O_3$	0.33	0.75	<1/2	35	3	4, 3, 2

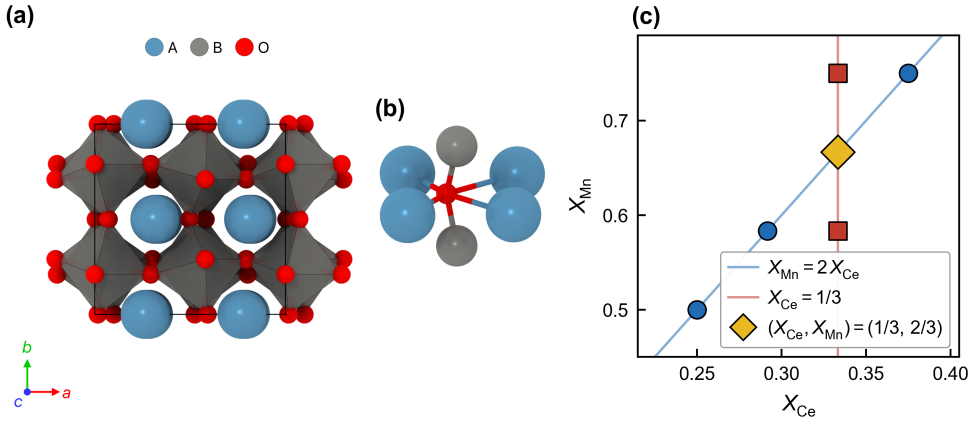


Fig. 1 (a) The ABO_3 perovskite host structure common to the CCTM compositions ($CaTiO_3$ cell, [001] projection), with A-site cations (blue) between corner-sharing BO_6 octahedra (B-site cations gray, O red). (b) Zoom on the local nearest-neighbor environment of a representative oxygen site (four A-site and two B-site coordinating cations). (c) Composition space explored, plotted as X_{Mn} vs. X_{Ce}. The blue line marks the charge-compensation condition $X_{Mn} = 2X_{Ce}$; the red line fixes $X_{Ce} = 1/3$. Blue circles and red squares denote the two compositional series, and the gold diamond marks their intersection, the reference composition CCTM2112. Compositions with $X_{Ce} > 1/3$ lie beyond the empirical Ce solubility limit, where CeO_2 exsolution is expected.[37,38]

Table 2 Summary statistics for oxygen-vacancy formation energies (E_v) across the six CCTM compositions. Means and medians are computed over all symmetry-distinct vacancy sites. "$E_v \leq 3.4$eV" and "$E_v \leq 3.9$eV" columns give the percentage of sites at or below each threshold; "In target range" is the percentage with $3.4 \leq E_v \leq 3.9$eV. Percentages rounded to nearest integer.

			Percent of sites with		Percent in
CCTM chemical formula	Mean	Median	$E_v \leq 3.4$eV	$E_v \leq 3.9$eV	target range
$Ca_{0.75}Ce_{0.25}Ti_{0.50}Mn_{0.50}O_3$	3.60	3.47	40	72	32
$Ca_{0.71}Ce_{0.29}Ti_{0.42}Mn_{0.58}O_3$	3.55	3.58	34	78	44
$Ca_{0.67}Ce_{0.33}Ti_{0.33}Mn_{0.67}O_3$	3.48	3.46	40	89	49
$Ca_{0.63}Ce_{0.37}Ti_{0.25}Mn_{0.75}O_3$	3.52	3.46	31	75	44
$Ca_{0.67}Ce_{0.33}Ti_{0.42}Mn_{0.58}O_3$	3.51	3.31	55	76	21
$Ca_{0.67}Ce_{0.33}Ti_{0.25}Mn_{0.75}O_3$	3.21	3.21	87	88	1

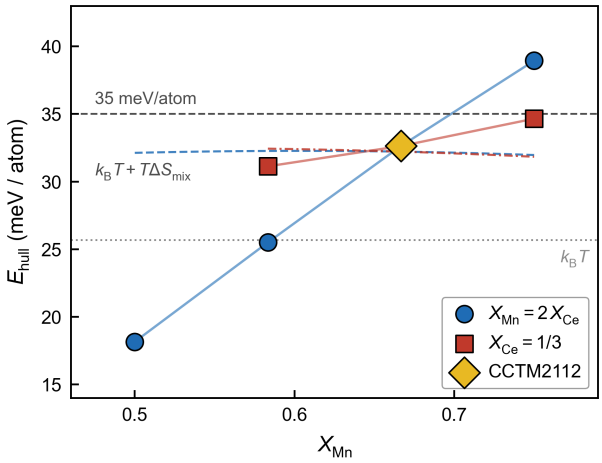


Fig. 2 Zero-kelvin energies above the convex hull (E_{hull}) for two CCTM compositional series: $X_{\mathrm{Mn}} = 2X_{\mathrm{Ce}}$ (charge-compensation line, blue circles) and $X_{\mathrm{Ce}} = 1/3$ (constant-Ce line, red squares); the gold diamond marks CCTM2112. Markers indicate 0 K E_{hull} in meV atom^{-1}. The dotted horizontal line marks the vibrational-entropy scale ($k_{\mathrm{B}}T$) at 298 K, the dashed horizontal line the empirical 35 meV atom^{-1} synthesizability threshold, and the blue dashed and red dash-dotted curves the combined vibrational and configurational-mixing offset ($k_{\mathrm{B}}T + T\Delta S_{\mathrm{mix}}$) at 298 K for each series (the two offset curves nearly coincide over the plotted range). These room-temperature reference scales are exceeded by several of the E_{hull} values; at the much higher synthesis temperature, the combined entropic offset is substantially larger and exceeds the E_{hull} values of all six compositions, indicating thermal accessibility.

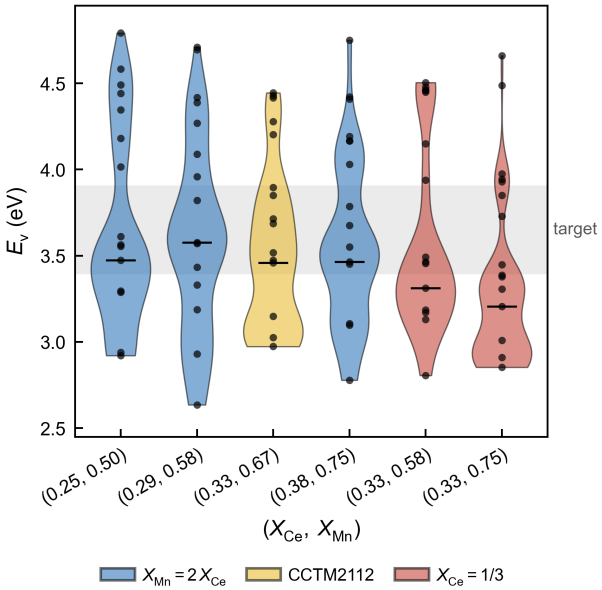


Fig. 3 Count-weighted distributions of oxygen-vacancy formation energies (E_{v}) for the six CCTM compositions, shown as violins at each (X_{Ce},X_{Mn}). Each violin is a kernel-density estimate over the symmetry-distinct vacancy environments weighted by their multiplicity; black bars mark the medians and black dots overlay the individual cell-mean E_{v} values. Violin fill color denotes the series: charge-compensation ($X_{\mathrm{Mn}} = 2X_{\mathrm{Ce}}$, blue), constant-Ce ($X_{\mathrm{Ce}} = 1/3$, red), and their intersection, CCTM2112 (gold). The gray shaded band denotes the target 3.4–3.9 eV window for balanced reduction–reoxidation cycling.

diverse oxides from intrinsic bulk properties (oxide formation enthalpy, midgap energy relative to the O 2p band center, and atomic electronegativity) to within ∼0.2 eV;[40] the crystal-feature model attains similar accuracy within the CCTM family using two descriptors chosen to expose the underlying Born–Haber thermochemistry. The fitted coefficients have a direct physical interpretation. Although $\langle E_{\mathrm{b}} \rangle$ and $\langle V_{\mathrm{r}} \rangle$ are each averaged over all six nearest neighbors, the coefficient $\beta_{\mathrm{b}} \approx 2.0$ indicates that approximately two bonds' worth of dissociation energy contributes to E_{v}, consistent with the two B-site cations forming direct M–O bonds to the removed oxygen, while the more distant A-site cations contribute primarily through electrostatics. Similarly, $\beta_{\mathrm{r}} \approx -1.3$ reflects stabilization of the two electrons released upon vacancy formation into redox-active states on neighboring cations. We evaluated E_{hull} as a third descriptor but excluded it from the final model: with only six unique E_{hull} values spanning a narrow range, its coefficient is not statistically resolved (the 95 % confidence interval spans zero), and including it does not improve the cross-validated error (ESI Table S3). This compact model directly encodes the underlying Born–Haber thermochemistry, enabling both rapid screening and mechanistic interpretation.

Cycle-level performance maps

The preceding section established how local cation chemistry controls E_{v}; here, we translate these site-level energetics into cycle-level performance. The local cation environments analyzed above produce a distribution of vacancy formation energies rather than a single characteristic value. For each local environment we compute the equilibrium probability that an oxygen site is vacant under representative reduction and oxidation conditions (eqn (4) in Methods); averaging this equilibrium vacancy population over the E_{v} distribution gives the oxygen off-stoichiometry δ (eqn (5)), and the difference between the reduction and oxidation states yields the cycle capacity, $\Delta\delta = \delta_{\mathrm{red}} - \delta_{\mathrm{ox}}$. The thermodynamic formalism (eqn (4) and (6)–(8) in Methods) treats vacancies as neutral and noninteracting, an approximation supported by the modest electrostatic coupling estimated in ESI Section S4. We compare predictions from the crystal-feature model (CFM) and the defect graph neural network (dGNN) across the CCTM composition space.

Crystal feature model.

The CFM gives a smooth, physically interpretable map of E_{v} across composition space. As shown in Fig. 5a, the predicted cycle capacity $\Delta\delta$ varies monotonically along the edges of the (X_{Ce}, X_{Mn}) composition square, increasing from the Ce-rich corner ($X_{\mathrm{Ce}} = 1$, $X_{\mathrm{Mn}} = 0$; $CeTiO_3$ limit) toward the Mn-rich corner ($X_{\mathrm{Ce}} = 0$, $X_{\mathrm{Mn}} = 1$; $CaMnO_3$ limit). This trend reflects the correlation between local Mn content and the favorable Mn^{4+}/Mn^{3+} reduction couple. For the cycle conditions employed here ($T_{\mathrm{red}} = 1350\,^{\circ}\mathrm{C}$, $P_{O_2} = 1 \times 10^{-4}$ bar; $T_{\mathrm{ox}} = 850\,^{\circ}\mathrm{C}$, $P_{H_2}/P_{H_2O} = 1 \times 10^{-3}$), the predicted cycle capacity $\Delta\delta$ spans 0–0.14 per formula unit across the accessible composition range. For comparison, ceria achieves $\Delta\delta/3 \approx 0.010$ under more aggressive cycling conditions

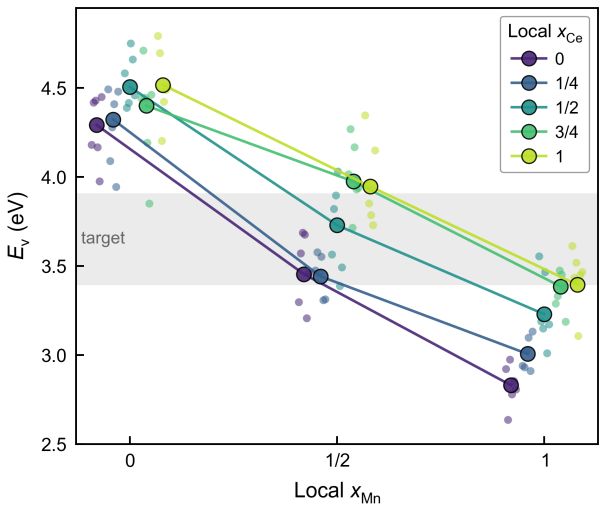


Fig. 4 Local-environment dependence of the oxygen-vacancy formation energy E_v. For each local nearest-neighbor composition (x_{Ce}, x_{Mn}), the E_v values from the six bulk compositions are shown as small markers; larger markers connected by lines give the count-weighted mean within each local-x_{Ce} series. The small markers are offset horizontally for visibility, both to separate the local-x_{Ce} color groups within each x_{Mn} position and to fan out the six bulk values within each cell; the underlying local x_{Mn} is exactly 0, 1/2, or 1, and the horizontal spread carries no information. Increasing the local Mn fraction lowers E_v (the dominant B-site effect), while the vertical separation between series at fixed x_{Mn} reflects the weaker A-site modulation with local Ce. The tight clustering of the six bulk markers within each cell indicates that the local-environment dependence is largely transferable across bulk compositions. The shaded band marks the target E_v window (3.4–3.9 eV) for solar thermochemical H_2 production.

($T_{red} \approx 1600\,^{\circ}C$, $P_{O_2} = 1 \times 10^{-5}$ bar; $T_{ox} \approx 900\,^{\circ}C$).[3] On a per-atom basis, $\Delta\delta$ is normalized by the number of atoms per formula unit: 5 for the ABO_3 CCTM perovskites and 3 for the CeO_2 fluorite that defines the $\Delta\delta/3$ ceria value above. On this basis, the synthesized CCTM compositions ($\Delta\delta/5 \approx 0.007$–$0.010$) approach or exceed this benchmark under our more moderate conditions, suggesting competitive performance with reduced thermal demands.

Practical synthesis constraints narrow the accessible region. Prior reports indicate that Ce solubility in the Ca–Mn–O perovskite host is limited, with CeO_2 segregating beyond the solubility limit,[37,38] and single-phase CCTM has been demonstrated up to $X_{Ce} = 1/3$ by powder X-ray diffraction;[30] our 0 K stability analysis additionally shows that compositions with $X_{Mn} \geq 0.75$ have E_{hull} values exceeding that of CCTM2112. These boundaries exclude a region at high Ce and high Mn on stability and solubility grounds. Within the remaining domain, the CFM predicts that $\Delta\delta$ is maximized near $X_{Ce} \approx 0$ and $X_{Mn} \approx 2/3$. Selecting this composition would forgo any potential kinetic or entropic benefits of A-site Ce, a tradeoff that merits experimental investigation.

Defect graph neural network.

Predictions from the dGNN are broadly consistent with the CFM but display nonmonotonic behavior along the $CaTiO_3$–$CaMnO_3$ and $CaMnO_3$–$CeMnO_3$ edges (Fig. 5b). Because the dGNN requires explicit structural input, we generated SQS supercells at 100 grid points across composition space and interpolated between them. The nonmonotonic features may reflect composition–structure–defect coupling that the linear CFM cannot capture, although some deviations could also arise from sparse sampling in certain composition regions. Without the stability constraint, the dGNN $\Delta\delta$ maximum lies near $(X_{Ce}, X_{Mn}) \approx (0.5, 1)$. When the E_{hull} and solubility constraints defined above are applied, compositions near $(X_{Ce}, X_{Mn}) \approx (0.22, 0.67)$ are favorable.

The CFM and dGNN give complementary descriptions of the CCTM redox behavior: the CFM represents mean thermodynamic trends with transparent physical interpretation, and the dGNN represents potential higher-order structure–composition–defect interactions. Composition ranges where the two predictions overlap balance reducibility with phase stability and are prioritized for experiment.

Experimental validation

We synthesized three CCTM compositions along the charge-compensation series at $X_{Ce} = 0.25$, 0.29, and 0.33, the last corresponding to CCTM2112 (full chemical formulas in Table 3), and measured their oxygen-exchange capacities by thermogravimetric analysis (TGA) and laser-heated stagnation flow reactor (LSFR) cycling. Only orthorhombic perovskite reflections were observed by powder X-ray diffraction for each of the three samples; in contrast to previous reports,[30] no CeO_2 or other secondary phase was detected. Laboratory XRD does not exclude nanocrystalline or amorphous CeO_2. Powder X-ray diffraction of the $X_{Ce} = 0.29$ sample after the four LSFR cycles of Fig. 6 and of CCTM2112 after 20 TGA cycles shows no secondary phases, decomposition, or structural changes relative to the as-synthesized patterns (ESI Section S5 and Fig. S6). We applied three TGA cycling protocols (A, B, and C; Experimental methods) and one LSFR protocol to test how reducing atmosphere and dwell time affect the measured $\Delta\delta$. Full TGA cycling traces and protocol details appear in ESI Section S6. Steady-state $\Delta\delta$ values are summarized in Table 3.

Under TGA Protocol C, in which the reduction P_{O_2} ($\approx 1.1 \times 10^{-3}$ bar) is closest to the model conditions, $\Delta\delta$ increases monotonically with X_{Ce} from 0.036 at $X_{Ce} = 0.25$ to 0.048 at $X_{Ce} = 0.33$. Under Protocols A and B, in which residual oxygen in the Ar carrier gives an effective $P_{O_2} \approx 1 \times 10^{-6}$ bar (substantially below the model conditions), measured $\Delta\delta$ is systematically higher (0.061–0.072) and the X_{Ce}-dependent ordering is preserved but flatter. Measured $\Delta\delta$ values are lower bounds on the equilibrium oxygen-exchange capacity in all four protocols, evidenced by the nonzero O_2 release rate at the end of the reduction step in the LSFR (Fig. 6). The specific rate-limiting step (surface exchange, bulk diffusion, or gas-phase transport) is not separately identified from the present data and likely differs across protocols owing to the different temperature ramps, atmospheres, and reactor geometries involved.

LSFR cycling of the $X_{Ce} = 0.29$ and 0.33 compositions yields steady-state $\Delta\delta$ values of 0.047 and 0.067, respectively, comparable to the corresponding TGA Protocol C values (0.044 and 0.048) despite the substantially shorter reduction dwell. This is consistent with laser heating reaching the reduction temperature faster than the TGA furnace ramp. Two features are apparent in the time-resolved O_2 and H_2 release rates (Fig. 6). First, the cycle-1

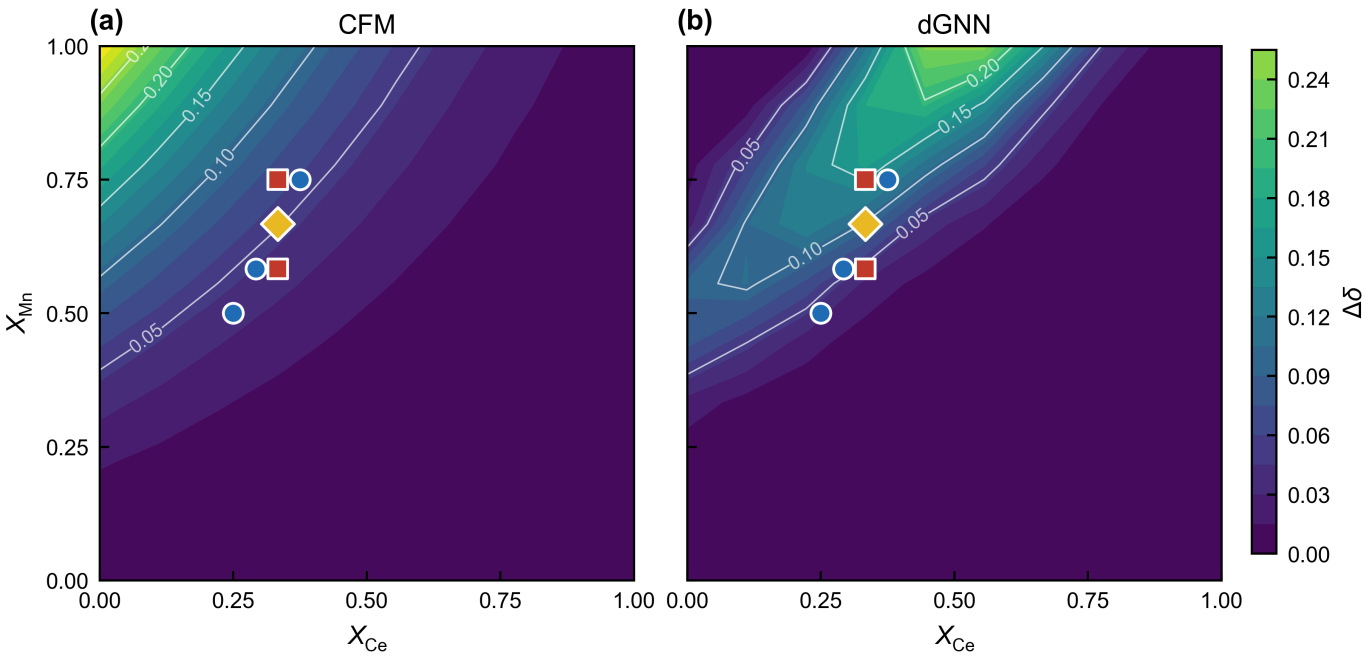


Fig. 5 Predicted oxygen-exchange capacity ($\Delta\delta$) across CCTM composition space from (a) the crystal-feature model (CFM) and (b) the defect graph neural network (dGNN). Axes denote bulk mole fractions X_{Ce} and X_{Mn}; the color scale indicates $\Delta\delta$, the exchanged oxygen per perovskite formula unit. White contours are spaced at intervals of 0.05 in $\Delta\delta$. Blue circles: charge-compensation series ($X_{Mn} = 2X_{Ce}$); red squares: constant-Ce series ($X_{Ce} = 1/3$); gold diamond: CCTM2112. The CFM surface increases monotonically toward the Mn-rich corner, whereas the dGNN surface exhibits a nonmonotonic ridge in mixed Ce–Mn regimes.

Table 3 Predicted and measured oxygen-exchange capacity ($\Delta\delta$) for three CCTM perovskites across cycling protocols. SCAN+U: site-resolved DFT vacancy formation energies for the 15 symmetry-distinct nearest-neighbor cation environments of each composition, weighted by their ideal-solution (binomial) probabilities at the bulk composition and evaluated through the thermodynamic formalism of ESI Section S7 (ESI eqn (S12) and (S14)). CFM: same binomial environment weighting applied to crystal-feature-model predictions of the per-environment E_v. dGNN: defect graph neural network ensemble-mean predictions on SQS supercells at 100 (X_{Ce}, X_{Mn}) grid points; off-grid compositions obtained by linear interpolation between the four nearest grid points. All three predictions use identical cycling conditions: $T_{red} = 1350\,°C$, $P_{O_2}^{red} = 1 \times 10^{-4}$ bar; $T_{ox} = 850\,°C$, $P_{H_2}/P_{H_2O} = 1 \times 10^{-3}$. TGA Protocol A: 1350 °C (0.5 h) / 1300 °C (1 h) reduction in Ar[a], 900 °C (0.5 h) reoxidation in 20 % O_2/Ar. Protocol B: 1350 °C (1 h) / 1300 °C (0.5 h) reduction in Ar[a]; same reoxidation. Protocol C: 1350 °C (1.5 h) reduction in 0.11 % O_2/Ar, 850 °C (1 h) reoxidation in the same atmosphere. LSFR: 1350 °C (5.5 min) reduction in Ar[a], 850 °C (25 min) reoxidation in 40 % H_2O/Ar; values are mean of cycles 2–4 from O_2 integration. Experimental uncertainties approximately ±10 %. Both TGA and LSFR $\Delta\delta$ are lower bounds on the equilibrium oxygen-exchange capacity owing to incomplete equilibration during the reduction dwell.

			Predicted			TGA Protocol				
Composition	X_{Ce}	X_{Mn}	SCAN+U	CFM	dGNN	A	B	C	LSFR	
$Ca_{0.75}Ce_{0.25}Ti_{0.50}Mn_{0.50}O_3$	0.25	0.50	0.043	0.036	0.042	0.061	0.066	0.036	—	[b]
$Ca_{0.71}Ce_{0.29}Ti_{0.42}Mn_{0.58}O_3$	0.29	0.58	0.069	0.044	0.058	0.066	0.071	0.044	0.047	
$Ca_{0.67}Ce_{0.33}Ti_{0.33}Mn_{0.67}O_3$	0.33	0.67	0.044	0.051	0.098	0.067	0.072	0.048	0.067	

[a] The Ar reduction atmosphere contains residual oxygen at $P_{O_2} \approx 0.1$–1 Pa ($\approx 1 \times 10^{-6}$–1×10^{-5} bar).
[b] LSFR not performed; the $X_{Ce} = 0.25$ composition is the least reducible in the experimental set.

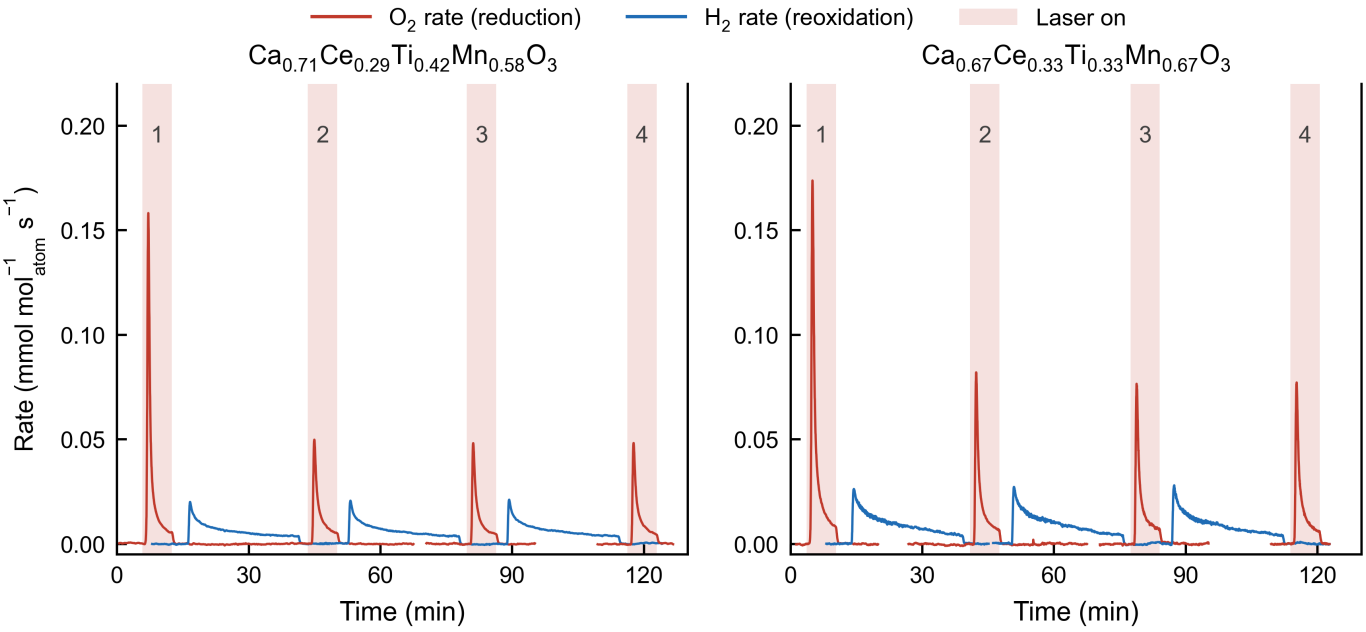


Fig. 6 Time-resolved oxygen and hydrogen release rates measured in the laser-heated stagnation flow reactor for $Ca_{0.71}Ce_{0.29}Ti_{0.42}Mn_{0.58}O_3$ ($X_{Ce} = 0.29$; left) and CCTM2112 ($X_{Ce} = 0.33$; right) over four redox cycles: O_2 release rate during reduction (red) and H_2 production rate during reoxidation (blue), normalized to total atoms in the perovskite formula unit. Shaded bands mark the intervals with the laser on, including its heating and cooling ramps; the laser-heated sample reached 1350 °C during each 5.5 min reduction under Ar. Reoxidation was carried out for 25 min under 40 % H_2O/Ar at 850 °C, set by the furnace control thermocouple. The cycle-1 O_2 peak exceeds the cycle-2–4 peaks by a factor of 2–3.3 in both compositions, reflecting preconditioning of as-synthesized material; tabulated $\Delta\delta$ values (Table 3) are averaged over cycles 2–4.

O_2 peak exceeds the cycle-2–4 peaks in both compositions; this behavior is commonly observed and motivates a redox break-in cycle, so tabulated $\Delta\delta$ values are averaged over cycles 2–4. The integrated gas amounts account for the larger first release. For CCTM2112, the O_2 released in cycle 1 corresponds to 0.120 O per formula unit, the subsequent steam reoxidation restored 0.072 O per formula unit (from the integrated H_2), and cycles 2–4 then released 0.066–0.069; for $X_{Ce} = 0.29$, the corresponding values are 0.092, 0.048, and 0.046–0.049. The as-synthesized powder was equilibrated with air, whereas in subsequent cycles the material is reoxidized in 40 % H_2O/Ar at 850 °C, a much weaker oxidant than air, so the first reduction also removes oxygen that steam does not restore. Second, the O_2 peak heights decrease slightly from cycle 2 to cycle 4, and the measured H_2/O_2 material balance shows a small (5–7 %) mismatch over time. Reoxidation of CCTM and related materials is much slower in water vapor (here 40 % H_2O) than in O_2/Ar mixtures such as those used in the TGA, so this trend is consistent with incomplete reoxidation to the starting state of the material in each cycle; the O_2 evolution is also truncated by the 5.5 min reduction window in each cycle. Both the peak-height decline and the material-balance mismatch therefore reflect an experimental artifact of reoxidation kinetics and cycle times rather than deactivation over consecutive cycles; a few-percent mass-spectrometer calibration uncertainty (certified gas standards; Experimental methods) may also contribute. This supports a kinetic rather than thermodynamic origin for the lower-bound character of the LSFR $\Delta\delta$ described above. The $X_{Ce} = 0.25$ composition was not measured in the LSFR because its predicted and TGA-measured $\Delta\delta$ are the lowest of the three compositions and below the productivity threshold of practical interest for subsequent characterization.

At cycling conditions close to the model conditions (TGA Protocol C, LSFR), measured $\Delta\delta$ at $X_{Ce} = 0.25$ (0.036) matches the CFM prediction (0.036) and lies below the SCAN+U and dGNN predictions (0.043 and 0.042, respectively). At CCTM2112 ($X_{Ce} = 0.33$), measured $\Delta\delta$ (0.048–0.067) brackets the CFM prediction (0.051); the SCAN+U value (0.044) lies just below the measured range, and the dGNN prediction (0.098) well above it. At $X_{Ce} = 0.29$, the SCAN+U (0.069) and dGNN predictions exceed the measured range (0.044–0.047) while the CFM (0.044) falls at the lower edge of the measured range, the closest of the three; the ordering is consistent with experimental $\Delta\delta$ being a lower bound on the equilibrium value, but the magnitude of the SCAN+U–experiment gap is larger here than at the other two compositions. Under Protocols A and B, measured $\Delta\delta$ exceeds all three predictions for all three compositions, consistent with the more strongly reducing residual-P_{O_2} atmospheres of these protocols falling outside the model conditions. Across the three compositions, the two fitted models deviate from SCAN+U in different ways: the CFM yields a narrower predicted $\Delta\delta$ range, while the dGNN yields a substantially larger $\Delta\delta$ at CCTM2112 (ESI Section S8.4). The implications of these complementary biases for fitted-model selection in composition-space screening are addressed in the Discussion.

Discussion

B-site chemistry as the primary control over vacancy energetics

Local B-site chemistry, not bulk stoichiometry alone, dominates oxygen-vacancy formation energetics in CCTM perovskites. Varying the Mn fraction among nearest-neighbor B sites shifts E_v by 1.0–1.5 eV depending on local Ce content, whereas A-site Ce variation produces a smaller, Mn-dependent shift of 0.2–0.6 eV (Fig. 4). This B-site shift is large relative to the targeted energetics: it spans 2–3 times the 0.5 eV width of the thermochemically favorable 3.4–3.9 eV window, and its upper end of 1.5 eV is 38–44 % of the target E_v itself. The larger B-site contribution suggests that short-range B-site cation order, rather than bulk composition, is the more effective target for tuning the E_v distribution: bulk optimization averages over local environments, whereas targeted B-site ordering could narrow the distribution and increase the fraction of sites within the thermochemically favorable 3.4–3.9 eV window. Adopting a uniformly narrow distribution as the optimization goal assumes that per-vacancy electronic entropy contributions are approximately uniform across local environments; differences between Ce- and Mn-localized vacancies could shift the optimum from a uniformly narrow distribution to one weighted toward specific local environments.

Several processing routes might achieve such control. Layer-by-layer thin-film growth could bias toward specific B-site ordering motifs; epitaxial strain, which couples to octahedral tilting and B–O bond lengths,[41,42] could indirectly bias cation arrangements through these structural distortions; thermal histories that permit partial B-site equilibration before quenching offer a bulk-compatible alternative; and aliovalent or size-mismatched dopants may promote B-site cation ordering directly in bulk material.[43,44] In related double perovskites, such substitution enhances B-site cation order, although the effect is system-dependent and the smaller B-site charge contrast in CCTM makes the outcome less certain. Any such order would be metastable, requiring kinetic trapping during synthesis, and could re-equilibrate toward the thermodynamically preferred arrangement at the high reduction temperatures of cycling; retention of the targeted ordering is therefore a prerequisite for this approach. The present work treats disordered configurations via SQS supercells; future first-principles calculations comparing representative ordered motifs to this baseline would quantify how much ordering can shift the E_v distribution and whether such shifts improve $\Delta\delta$ without compromising phase stability. Such ordering can be quantified by short-range order parameters (e.g., Warren–Cowley pair correlations[45,46] on the B-site Ti–Mn sublattice, with secondary parameters describing A-site Ca–Ce mixing and the cross-sublattice Ce–Mn correlation, extended to multiple sublattices in standard fashion[47]), which are measurable by high-resolution electron microscopy and can be computed from the same supercell configurations used to evaluate the E_v distribution.

The larger B-site contribution to E_v is reflected in the CFM coefficients, whose fitted values ($\beta_b \approx 2.0$, $\beta_r \approx -1.3$) recover the direct M–O bonding of the two B-site cations to the removed oxygen and the stabilization of the two released electrons, as detailed above. Substituting Mn for Ti weakens the M–O bonds and provides a more favorable reduction couple (Mn^{4+}/Mn^{3+} vs. Ti^{4+}/Ti^{3+}), both of which lower E_v.[48,49] The smaller influence of A-site Ce likely reflects the interplay between Ce's reduction potential, which is intermediate between the more reducible Mn^{4+}/Mn^{3+} and the less reducible Ti^{4+}/Ti^{3+} couples, and local structural distortions, though a full mechanistic decomposition remains an open question; the sense in which Ce can be both Ce^{3+}-like and electronically active in reduction is addressed below.

Cerium oxidation states and delocalized reduction

SCAN+U predicts predominantly Ce^{3+}-like character in pristine CCTM; this assignment has not been verified experimentally for the present compositions. In the CCTM2112 supercell, 23 of 24 Ce sites have calculated moments of 0.45–0.85 μ_B, below the 0.94 μ_B of fully localized Ce^{3+} in Ce_2O_3 in the same framework, which indicates fractional $4f$ occupation closer to $4f^1$ than to $4f^0$ (ESI Fig. S1 and Table S1). Although the pristine compositions thus exhibit predominantly Ce^{3+}-like character within the SCAN+U description, the changes in Ce $4f$ occupation that accompany vacancy formation (below) show that Ce remains electronically active during reduction and reoxidation, participating in charge compensation through redistribution of electronic density rather than through a discrete $Ce^{4+} \rightarrow Ce^{3+}$ transition. This finding contrasts with earlier work emphasizing $Ce^{4+} \rightarrow Ce^{3+}$ reduction as a primary contributor to redox activity.[30] Both studies used 360-atom SQS supercells, and starting from the initial magnetic moments of the earlier work recovers the Ce^{3+}-like state at fixed geometry (ESI Section S1), so the origin of this difference is not established; it may reflect the different cation configurations of the two SQS realizations or their relaxed structures. The experimental evidence on Ce and Mn oxidation states in CCTM is limited to soft X-ray absorption spectroscopy (XAS) of CCTM2112 prepared by solid-state reaction,[30] which found predominantly Ce^{4+} and Mn^{3+} in the oxidized material and, on reduction, a reversible decrease of the average Ce oxidation state to 3.90(3) with a small net change in Mn. The delocalized-reduction picture described below is therefore a result of the SCAN+U description that remains to be tested experimentally for the present compositions. Reduction can still occur at Ce^{3+}-like sites: the partially occupied Ce $4f$ states are near the Fermi level, providing a manifold that accommodates the electrons released on vacancy formation, distributing a small additional reduction over many Ce^{3+}-like sites rather than driving a discrete change in the formal oxidation state of any single Ce ion.[6] Nonlocal accommodation of the electrons released upon oxygen-vacancy formation has precedent in related perovskites: in $SrFeO_{3-\delta}$, these electrons localize on second-nearest-neighbor Fe rather than the directly coordinated cation.[50]

In all six compositions, the vacancy-induced changes in the calculated local magnetic moments occur on Ce and Mn, with smaller induced moments on O, whereas individual Ti and Ca moments change by less than 0.05 μ_B (ESI Table S2). Averaged over the 15 vacancies of each composition, the net change in the Ce moment magnitudes, summed over the Ce sites, is 0.55–0.94 μ_B, and that of Mn is 0.52–0.70 μ_B in five of the six compositions, rising to 1.13 μ_B in the most Ce-rich composition ($X_{Ce} = 0.37$).

For CCTM2112, the net Ce and Mn changes are similar (0.70 and 0.65 μ_B), whereas the XAS placed most of the net reduction on Ce.[30] These moment changes are computational indicators of the redox response, not a measure of electron transfer.

Resolving the precise partitioning of reduction between Ce and Mn will require further investigation. Local compositional fluctuations, combined with the sensitivity of oxidation-state assignments to the choice of DFT functional and Hubbard U parameters, complicate definitive mechanistic attribution. For thermochemical screening purposes, however, the key point is that the CFM and dGNN capture the net effect of these contributions on E_v without requiring a complete mechanistic decomposition, an advantage for high-throughput materials discovery.

Model validation and limitations

The CFM and dGNN deviate from SCAN+U (the DFT reference in Table 3) in different ways. The CFM's predicted $\Delta\delta$ range across the three measured compositions (0.036–0.051) is narrower than that of SCAN+U (0.043–0.069); this is consistent with the linear functional form of the CFM, which cannot represent composition-specific changes in the shape of the underlying E_v distribution, whose low-E_v tail governs the Boltzmann average. The dGNN agrees with SCAN+U within 16 % at $X_{Ce} = 0.25$ and 0.29 but predicts substantially larger $\Delta\delta$ at CCTM2112 (0.098 vs. SCAN+U 0.044); we attribute this to a broader, lower-E_v tail of the dGNN E_v distribution at this composition (ESI Section S8.4). At $X_{Ce} = 0.29$, the SCAN+U value (0.069) exceeds both fitted-model predictions and the measured range (0.044–0.047); the present data do not distinguish whether this reflects composition-specific incomplete equilibration in the experiment, a nonrepresentative low-E_v tail in the 15-site DFT sample, or both. The spread among the three predictions defines an effective uncertainty band for composition-space screening: within its training composition window the CFM tends to give a conservative (typically lower) $\Delta\delta$ estimate, lying below SCAN+U at two of the three measured compositions (the exception being CCTM2112). Compositions with large dGNN–SCAN+U disagreement warrant cross-checking with SCAN+U before committing to synthesis.

Two further caveats qualify this comparison. First, the noninteracting vacancy approximation does not include possible vacancy–vacancy clustering at high δ; electrostatic repulsion remains modest (a few tens of meV) over the relevant δ range, per the screened-monopole analysis in ESI Fig. S4, but short-range chemical interactions could modify the effective E_v distribution at elevated defect concentrations. Second, the dGNN screening surface (Fig. 5b) exhibits nonmonotonic features in composition regions outside the measured set; the present validation cannot distinguish whether these reflect genuine composition–structure coupling captured by the dGNN's structural input or sparse-sampling artifacts of the underlying training data. Expanding the SCAN+U data set or the dGNN training set with additional CCTM compositions, particularly in the mixed Ce–Mn regime at intermediate X_{Ce}, would help discriminate between these possibilities.

The thermodynamic model includes the gas-phase entropy, through the oxygen chemical potential, and the configurational entropy of the vacancies, through the lattice-gas occupations; the latter depends on composition through the distribution of E_v over the fifteen local environments. The model omits the vibrational entropy of the solid, which harmonic-phonon calculations for related Mn-containing perovskites show to be smaller than the gas-phase and configurational contributions,[51] and the electronic entropy, whose magnitude depends on how the released electrons are distributed over the Ce 4f and Mn 3d states. A composition-dependent electronic entropy would shift the predicted $\Delta\delta$ and could favor E_v distributions weighted toward particular local environments.

Outlook and transferability

The interpretable modeling framework developed here provides design principles that should transfer to related perovskite families. The finding that B-site chemistry dominates E_v suggests that other systems with mixed B-site occupancy, such as Sr–Ce–Mn–O or Ba–Ce–Mn–O analogs, may exhibit similar tunability through short-range cation order.[26,38,52] The Born–Haber decomposition represented by the CFM coefficients (bond-breaking vs. reduction stabilization) provides a physically grounded basis for predicting how alternative dopants will shift the E_v distribution: species with weaker M–O bonds or more favorable reduction couples should lower E_v, while the opposite perturbations should raise it.

Extending this approach to new compositions requires generating appropriate SQS supercells, computing E_v for representative local environments, and optionally fine-tuning the dGNN on the expanded dataset. The computational cost is modest, roughly 16 DFT calculations per composition for complete coverage of the 15 nearest-neighbor environments, making systematic screening across multi-cation perovskite spaces tractable. We note that the present analysis addresses thermodynamic capacity; practical performance also depends on oxygen-transport kinetics and surface-exchange rates, which merit complementary investigation. The reoxidation measurements reported here were performed in steam (40 % H_2O/Ar, with no added H_2); CCTM performance under high H_2/H_2O ratios, the stricter and more commercially relevant reoxidation test, is left for future work. Element-specific measurements on the synthesized compositions, such as Ce and Mn X-ray absorption spectroscopy before and after reduction, would test the calculated partition of reduction between Ce and Mn, which has not been verified experimentally for these compositions.

Conclusions

This work establishes an interpretable computational framework for mapping oxygen-vacancy formation energetics across compositionally complex perovskites. Using a coverage-constrained special quasirandom structure methodology that samples all fifteen symmetry-distinct oxygen nearest-neighbor environments, we computed vacancy formation energies for six Ca–Ce–Ti–Mn compositions and developed two complementary fitted models: a crystal-feature model (CFM) whose fitted coefficients directly encode the underlying Born–Haber thermochemistry, and a fine-tuned defect graph neural network (dGNN) that models potential nonlinear structure–composition–defect coupling beyond the

linear form of the CFM. Vacancy formation energetics in CCTM are dominated by local B-site chemistry: changing the nearest-neighbor Mn fraction shifts E_v by 1.0–1.5 eV depending on local Ce content, whereas A-site Ce variation produces a smaller, Mn-dependent shift of 0.2–0.6 eV. This hierarchy indicates that short-range B-site cation order, if it can be established and kinetically retained through processing, is a candidate means of tuning redox performance. Composition-space maps show a Ce/Mn-balanced region ($X_{Ce} \approx 0.29$–0.33, $X_{Mn} \approx 0.58$–0.67) that combines a high in-window E_v fraction with phase stability and solubility, where the predicted cycle capacity $\Delta\delta$ is comparable to or exceeds the ceria benchmark ($\Delta\delta/3 \approx 0.010$) at substantially lower reduction temperatures ($T_{red} = 1350\,^{\circ}\mathrm{C}$ vs. $\sim 1600\,^{\circ}\mathrm{C}$ for ceria).[3] Experimental measurements on three compositions along the charge-compensation line $X_{Mn} = 2X_{Ce}$ show $\Delta\delta$ increasing monotonically with X_{Ce} under cycling protocols close to the model conditions, consistent with the qualitative trend from the fitted models; the measured $\Delta\delta$ values exceed the model predictions under more strongly reducing protocols. The interpretable framework provides compositional screening capability and mechanistic design rules expected to transfer to related perovskite families for solar thermochemical hydrogen production.

Methods

Computational and theoretical methods

Supercell construction and vacancy site selection.

To model configurational disorder in the CCTM solid solution, we generated special quasirandom structures (SQSs)[53,54] using the ICET package.[55] A 360-atom orthorhombic $3 \times 3 \times 2$ supercell was constructed with initial lattice parameters $a = 16.12$ Å, $b = 16.39$ Å, and $c = 15.27$ Å; lattice vectors and internal coordinates were subsequently relaxed by DFT for each composition. Additional SQS methodology details and prior validation for multication perovskites are provided in ref. 30. The cluster space was defined with pair and triplet cutoffs of 7.0 Å and 4.0 Å (ICET v2.2; symmetry tolerance 10^{-4}), and the SQS were optimized by 100 001 Monte Carlo trial steps (optimality weight 1) from a fixed random seed; the realized supercells are provided in the data release.

The default SQS objective in ICET does not ensure that every symmetry-distinct oxygen first-nearest-neighbor (1NN) environment is realized. In CCTM, the four A-site and two B-site neighbors surrounding each oxygen yield up to fifteen symmetry-distinct 1NN environments. To promote complete coverage, we augmented the SQS objective with a penalty term:

$$Q' = Q + k\,|15 - N_{env}|, \tag{2}$$

where Q and Q' are the original and modified objectives, N_{env} is the number of distinct O-site 1NN environments realized in the supercell, and k is a penalty factor. Setting $k = 2000$ reliably produced SQS cells containing all fifteen environments. The coverage constraint also removes a source of uncontrolled variance in computed bulk energetics, since standard SQS realizations at the same composition can sample different 1NN environment subsets; ESI Section S9 estimates the magnitude of this variance for CCTM2112 by comparison with the standard-SQS realization of ref. 30.

Having generated supercells with complete 1NN coverage, we next selected representative vacancy sites for DFT calculations. Each 360-atom supercell contains 216 oxygen sites, of which 15 are symmetry-distinct by 1NN environment. To avoid redundant calculations, we created one neutral oxygen vacancy per environment class. The representative site within each class was chosen from a two-dimensional Gaussian kernel density estimate (SCIPY `gaussian_kde`,[56] bandwidth 0.5) of the second-shell Ce and Mn cation fractions among all O sites sharing that 1NN environment; the site nearest the density maximum was designated as the representative vacancy, so that each selected site is statistically typical of its class. For classes containing two or fewer sites, the first such site was used.

Density functional theory calculations.

All calculations were performed with spin-polarized DFT using the Vienna ab initio simulation package (VASP) v5.4.4 and the projector-augmented-wave (PAW) formalism. The PAW potentials, from the standard `PAW_PBE` dataset, treated the valence configurations Ca $3s^2 3p^6 4s^2$ (`Ca_sv`), Ce $5s^2 5p^6 6s^2 4f^1 5d^1$ (`Ce`, with the $4f$ states in the valence), Ti $3p^6 3d^2 4s^2$ (`Ti_pv`), Mn $3p^6 3d^5 4s^2$ (`Mn_pv`), and O $2s^2 2p^4$ (`O`). We employed the SCAN exchange–correlation functional with Hubbard U corrections (SCAN+U) to account for onsite correlation in transition-metal and f-electron states, adopting $U_{Ce} = 2.0$ eV, $U_{Ti} = 2.5$ eV, and $U_{Mn} = 2.7$ eV based on prior benchmarks against experimental oxidation enthalpies.[57,58] The corrections used the rotationally invariant (Dudarev) scheme (`LDAUTYPE = 2`) with $J = 0$, so the quoted values are effective $U_{eff} = U - J$ applied to the Ce $4f$, Ti $3d$, and Mn $3d$ states, with `LMAXMIX = 6`. The plane-wave energy cutoff was 520 eV, and Brillouin-zone sampling was restricted to the Γ point, given the large supercell size. All calculations used the `Accurate` precision setting and the aspherical-gradient correction (`LASPH = True`) required for the meta-generalized gradient approximation. Total energies were minimized with the all-bands algorithm (`ALGO = All`) to an electronic self-consistency threshold of 10^{-5} eV (`EDIFF`) using Gaussian smearing (`ISMEAR = 0`) with a width of 0.05 eV, with symmetry disabled (`ISYM = 0`). The pristine supercells were relaxed with respect to both cell and ionic degrees of freedom (`ISIF = 3`); each defective supercell was then relaxed at the fixed pristine cell shape and volume, allowing only the ions to move (`ISIF = 2`). Both used a quasi-Newton algorithm (`IBRION = 1`) with an ionic force threshold of 0.03 eV Å^{-1} (`EDIFFG = -0.03`). Collinear spin polarization was applied with ferromagnetic initial states; initial magnetic moments were set to $0.6\,\mu_B$ on Ca and Ti and to $1.0\,\mu_B$ and $5.0\,\mu_B$ on Ce and Mn, respectively, then allowed to relax self-consistently.

The chemical and magnetic disorder in these 360-atom cells precludes exhaustive enumeration of magnetic orderings or systematic U-parameter sweeps. Prior work indicates that compositional rankings by E_v are robust to moderate U variations despite U-dependent absolute values,[59] and that magnetic energy scales are typically smaller than redox energetics in transition-metal perovskite oxides.[60] A more comprehensive treatment of magnetic disorder, such as disordered-local-moment averaging, is left for future work.

Site-resolved magnetic moments were obtained by integrating the spin density ($\rho_\uparrow - \rho_\downarrow$) within PAW spheres; Bader moments[61,62] for representative structures confirm robustness to the partition choice (ESI Section S1). Thermodynamic stability was assessed via the 0 K energy above the convex hull (E_{hull}), computed with the PYMATGEN `PhaseDiagram` module.[63–65] The hull was constructed from a reference set of elemental, binary, and ternary phases spanning the Ca–Ce–Ti–Mn–O system, with total energies taken from our prior work[29,34,57,58] at the same SCAN+U level as the CCTM supercells (elemental metals at the SCAN level), so that no cross-functional energy correction is applied; E_{hull} is the energy of each composition above this hull. Density of states calculations used Gaussian smearing (0.05 eV width) at the Γ point; a $2\times2\times2$ k-mesh produced no qualitative differences (ESI Fig. S11).

The partially occupied Ce $4f$ states cross the Fermi level in all six compositions, resulting in metallic electronic structure (ESI Fig. S2). In such metallic hosts, positively charged oxygen vacancies are disfavored because excess electrons are readily accommodated in the conduction manifold;[66] we therefore treat neutral vacancies as the relevant charge state, consistent with the computed metallic electronic structure of all compositions studied.

Neutral oxygen-vacancy formation energies were computed as

$$E_{\mathrm{v}} = E(\mathrm{defective}) - E(\mathrm{pristine}) + \frac{1}{2}E_{\mathrm{O_2}}, \tag{3}$$

where $E(\mathrm{defective})$ and $E(\mathrm{pristine})$ are the total energies of the vacancy-containing and stoichiometric supercells, respectively.

Thermodynamic modeling.

To translate oxygen-vacancy formation energies into cycle-level performance metrics, we modeled the equilibrium oxygen off-stoichiometry $\delta(T,\mu_{\mathrm{O}})$ under representative thermochemical cycling conditions. The lattice is treated as a set of oxygen sites that are either occupied or vacant. For neutral, noninteracting vacancies with temperature-independent formation energy $E_{\mathrm{v}}(\mathbf{x},\mathbf{X})$, where $\mathbf{x}=(x_{\mathrm{Ce}},x_{\mathrm{Mn}})$ denotes the local 1NN environment and $\mathbf{X}$ the bulk composition, the probability that a site is vacant at temperature T and oxygen chemical potential μ_{O} is

$$n(\mathbf{x},\mathbf{X}) = \frac{1}{1+\exp\left[\frac{E_{\mathrm{v}}(\mathbf{x},\mathbf{X})+\mu_{\mathrm{O}}(T,\{P_i\})}{k_{\mathrm{B}}T}\right]}. \tag{4}$$

The overall oxygen deficiency follows from averaging over all local environments,

$$\delta(T,\mu_{\mathrm{O}}) = 3\langle n(\mathbf{x},\mathbf{X})\rangle, \tag{5}$$

where the factor of 3 reflects the three oxygen atoms per ABO_3 formula unit.

During thermal reduction, the oxide equilibrates with O_2(g), and the oxygen chemical potential per atom is

$$\mu_{\mathrm{O}}(T,P_{\mathrm{O_2}}) = \frac{1}{2}\left[\mu^{\circ}_{\mathrm{O_2}}(T) + k_{\mathrm{B}}T\ln\left(\frac{P_{\mathrm{O_2}}}{P^{\circ}}\right)\right], \tag{6}$$

where $\mu^{\circ}_{\mathrm{O_2}}(T)$ is the standard chemical potential of O_2 from NIST-JANAF thermochemical tables[67] and $P^{\circ}=1$ bar. All oxygen chemical potentials are referenced to the SCAN total energy of O_2, computed for a spin-triplet molecule in a 15 Å cubic cell at the Γ point with the same functional, cutoff, and smearing as the solids. No empirical O_2 energy correction is applied: SCAN reproduces the O_2 equilibrium bond length (1.22 Å vs. the experimental 1.208 Å) and yields a dissociation energy of 5.28 eV, consistent with its benchmarked molecular accuracy,[68] and in any case the O_2 reference energy cancels between E_{v} and the oxygen chemical potential (ESI Section S7), so its absolute value does not affect the computed $\Delta\delta$. The connection between 0 K DFT E_{v} and the finite-temperature formulation is derived in ESI Section S7.

During water splitting, the relevant equilibrium is

$$\mathrm{H_2(g)} + \mathrm{O_{lattice}} \rightleftharpoons \mathrm{H_2O(g)}, \tag{7}$$

with corresponding oxygen chemical potential

$$\mu_{\mathrm{O}}(T,P_{\mathrm{H_2O}},P_{\mathrm{H_2}}) = \mu^{\circ}_{\mathrm{H_2O}}(T) - \mu^{\circ}_{\mathrm{H_2}}(T) + k_{\mathrm{B}}T\ln\left(\frac{P_{\mathrm{H_2O}}}{P_{\mathrm{H_2}}}\right). \tag{8}$$

Substituting eqn (6) into eqn (4) and averaging via eqn (5) yields the equilibrium deficiency during reduction, $\delta_{\mathrm{red}}(T_{\mathrm{red}},P_{\mathrm{O_2}})$; substituting eqn (8) yields the oxidation deficiency, $\delta_{\mathrm{ox}}(T_{\mathrm{ox}},P_{\mathrm{H_2O}}/P_{\mathrm{H_2}})$. The cycle capacity is $\Delta\delta = \delta_{\mathrm{red}} - \delta_{\mathrm{ox}}$. For the screening calculations, we used $T_{\mathrm{red}} = 1350\,^{\circ}$C, $P_{\mathrm{O_2}} = 1\times10^{-4}$ bar; $T_{\mathrm{ox}} = 850\,^{\circ}$C, $P_{\mathrm{H_2O}}/P_{\mathrm{H_2}} = 1000$ (i.e., $P_{\mathrm{H_2}}/P_{\mathrm{H_2O}} = 1\times10^{-3}$). These conditions are representative of those used in prior solar thermochemical measurements on Sr–La–Mn–Al (SLMA) and Ba–Ce–Mn (BCM) perovskites, ceria, and CCTM2112,[26,30] and are adopted here for comparability rather than as a CCTM-specific optimum.

To map $\Delta\delta$ across the full CCTM composition space, we replaced DFT E_{v} values with CFM or dGNN predictions. For the dGNN, which requires explicit structural input, we generated SQS supercells at 100 grid points and linearly interpolated for off-grid compositions.

Model construction.

Crystal feature model. The crystal-feature model (CFM) uses two physically motivated descriptors: the average metal–oxygen bond-dissociation energy $\langle E_{\mathrm{b}}\rangle$ and the average crystal reduction potential $\langle V_{\mathrm{r}}\rangle$. Both $\langle E_{\mathrm{b}}\rangle$ and $\langle V_{\mathrm{r}}\rangle$ are computed by averaging tabulated atomic values (ESI Tables S6 and S7) over all six nearest-neighbor cations surrounding the vacancy (four A-site, two B-site), reflecting the local chemical environment. Because all CCTM compositions exhibit metallic electronic structure, band gap is not included as a feature.

Model coefficients were obtained by Huber regression,[69,70] which provides robust estimates for datasets with heterogeneous variance. The reported coefficients are obtained from a single Huber fit to the full 90-site dataset, with 95 % confidence intervals from bootstrap resampling of sites with replacement (2000 resamples). Prediction accuracy is assessed separately by 1000 random 50 %/50 % train–test splits and by leave-one-composition-out cross-validation, both reported in ESI Section S3. The fitted coefficients ($\beta_{\mathrm{b}}\approx2.0$, $\beta_{\mathrm{r}}\approx-1.3$, $\beta_0\approx-4.26$) and their physical interpretation are discussed in the Results.

Defect graph neural network model. We validated and extended the defect graph neural network (dGNN) approach previously developed by Witman et al.[35] by testing it on CCTM oxygen-

vacancy formation energies. The original dGNN training data ("Base" dataset) consisted primarily of binary and ternary oxides, with limited quaternary compounds; it has since been augmented with additional quaternary oxides and ABO_3 perovskite data from ref. 34. The CCTM system lies outside the chemical space of the Base training data and contains O nearest-neighbor environments absent from that data. To improve predictions, we constructed a fine-tuning (FT) dataset by augmenting the Base data with 20 % of the CCTM vacancy energies computed in this work.

Model architecture and training hyperparameters are described in ESI Section S8. Using K-fold cross-validation, each E_v is predicted by an ensemble of K models; the ensemble mean provides the final prediction, and the standard deviation serves as an uncertainty estimate. ESI Fig. S8 compares parity plots for the Base and FT models: the Base model performs reasonably on the CCTM hold-out set, but fine-tuning substantially reduces both error and uncertainty.

To screen across composition space, we generated SQS supercells at 100 grid points spanning the (X_{Ce}, X_{Mn}) domain and predicted E_v distributions for each. The resulting distributions (ESI Fig. S9 and S10) indicate composition-dependent nonlinearity in the dGNN predictions and notable variation in E_v spread. These distributions were used to compute $\delta(T, \mu_O)$ via eqn (5).

Experimental methods

Synthesis.

We synthesized CCTM samples by a modified Pechini route.[71] We dissolved stoichiometric amounts of titanium bis(ammonium lactato)dihydroxide (TALH; 50 % (w/w) in H_2O) and the acetates of calcium, cerium, and manganese in deionized water with citric acid as a chelating agent (1:3 metal-cation to citric-acid molar ratio); all reagents were obtained from Sigma-Aldrich (cerium acetate, 99.9 % trace-metals basis; calcium acetate and citric acid, ≥99.0 %; manganese acetate, ≥99 %). We evaporated the solution to dryness in an oven at 150 °C for 15 h, ground the resulting gel to a coarse powder, and calcined this powder at 1000 °C for 6 h in static air (heating rate 3 °C min^{-1}). We pressed the calcined powder in a 6.35 mm die at 2.5 MPa, pre-fired the resulting pellets at 1000 °C for 6 h in air, and sintered them at 1425 °C (1450 °C for CCTM2112) for 6 h in static air on CeO_2 coasters (to prevent reaction with the crucible) using a three-stage ramp (2.5 °C min^{-1} to 850 °C, 2.25 °C min^{-1} to 1300 °C, 1.25 °C min^{-1} to the sintering temperature), and ground the sintered pellets to a fine powder using a mortar and pestle for subsequent characterization. The reported compositions are nominal cation stoichiometries; analyzed compositions will be reported separately.[72] Within the CFM, a deviation of 0.01 in X_{Ce} or X_{Mn} from the nominal composition changes the predicted $\Delta\delta$ of the three synthesized compositions by at most 0.002, less than the experimental uncertainty.

X-ray diffraction.

We characterized phase purity by powder X-ray diffraction (XRD) on a Malvern Panalytical Aeris powder diffractometer with Cu Kα radiation (40 kV, 15 mA; Kα_2 not stripped, $I_{K\alpha_2}/I_{K\alpha_1} = 0.5$) in Bragg–Brentano geometry, without a secondary monochromator and with a fixed 0.76 mm divergence slit. Powder samples were mounted on a zero-background silicon holder and scanned in continuous mode over 2θ = 5–90° with a step size of 0.0217° and an effective counting time of 25.2 s per step (3911 points per scan). The calculated reference pattern shown in ESI Section S5 was generated from a 360-atom $3 \times 3 \times 2$ SQS supercell of CCTM2112 using the `XRDCalculator` module of PYMATGEN.[65]

TGA measurements.

We measured oxygen uptake and release on a NETZSCH STA 449 F3 Jupiter thermogravimetric analyzer equipped with a graphite furnace. Carrier gases were ultra-high-purity Ar (99.99 %) for Protocols A and B and a certified 1102 ppm O_2-in-Ar standard (nominal 0.11 % O_2/Ar, $P_{O_2} = 1.1 \times 10^{-3}$ bar) for Protocol C. For each measurement, we loaded 80 mg of CCTM powder into a calcia-stabilized zirconia crucible and heated the sample at 10 °C min^{-1} to the reduction temperature under flowing carrier gas at a total flow rate of 50 mL min^{-1}. The three TGA protocols differed in reduction atmosphere, reduction dwell-time partition, and reoxidation conditions. In Protocol A, samples were reduced at 1350 °C (0.5 h) followed by 1300 °C (1 h) under flowing Ar and reoxidized at 900 °C (0.5 h) under 20 % O_2/Ar. Protocol B used the same atmospheres and reoxidation conditions as Protocol A but exchanged the two reduction-step durations to 1350 °C (1 h) followed by 1300 °C (0.5 h). In both two-step protocols, the initial step at the higher 1350 °C accelerates the approach to the reduction equilibrium at 1300 °C, which is otherwise slow to reach at that temperature alone. In Protocol C, samples were reduced at 1350 °C (1.5 h) under 0.11 % O_2/Ar and reoxidized at 850 °C (1 h) under the same atmosphere. Each protocol comprised five reduction–reoxidation cycles; reported $\Delta\delta$ values are means over cycles 2–5, with cycle 1 excluded to avoid preconditioning effects (see Experimental validation). Apparent sample-mass changes were corrected for buoyancy by subtracting an empty-crucible blank acquired under the same temperature and gas program before conversion. We converted the corrected mass change to oxygen off-stoichiometry δ assuming

$$\delta = \left(\frac{\Delta m}{m_{\text{initial}}}\right)\left(\frac{\text{MW}_{\text{CCTM}}}{\text{MW}_{\text{O}}}\right), \tag{9}$$

where Δm is the measured mass change, m_{initial} is the initial sample mass, and MW_{CCTM} and MW_{O} are the molecular weights of the oxide and atomic oxygen, respectively. Experimental uncertainty in $\Delta\delta$ is approximately ±10 %, dominated by uncertainty in the residual P_{O_2} (∼1 Pa) in the Ar carrier supply for Protocols A and B.

LSFR measurements.

We measured oxygen-release and hydrogen-production rates on the Sandia National Laboratories laser-heated stagnation flow reactor (LSFR),[13,73–75] in which samples are heated rapidly by focused continuous-wave laser irradiation. For each measurement, we loaded 80–100 mg of CCTM powder onto a platinum foil supported on a zirconia sample holder; sample-surface temperature was measured by a two-color pyrometer (Process Sensors PYROSPOT DGR 55N) positioned directly above the sample. The pyrometer was calibrated against a tube-furnace control thermo-

couple as the temperature standard: at 1400 °C its reading was matched to the thermocouple, and the agreement was verified at other temperatures; the emissivity was set to 1 with a two-color correction factor of 1.004. Before cycle 1, the furnace and sample were preheated to 850 °C under Ar; every reduction, including the first, was driven from 850 °C to 1350 °C by the laser. We reduced samples at 1350 °C for 5.5 min under flowing Ar at a total flow rate of 300 mL min^{-1}. We then cooled to 850 °C and reoxidized for 25 min under 40 % H_2O/Ar at a total flow rate of 500 mL min^{-1} (300 mL min^{-1} Ar carrier + 200 mL min^{-1} H_2O). The furnace control thermocouple, which sets the reoxidation temperature, read 850.0(5) °C throughout every reoxidation step; at this set point, the pyrometer read 852–855 °C under Ar but 873–877 °C while the H_2O/Ar reoxidation gas was flowing, an offset of approximately 20 °C that appears in every cycle as a step when the steam flow starts. Reactor effluent was sampled continuously by a downstream Extrel C50 modulated effusive-beam quadrupole mass spectrometer. The O_2 and H_2 signals were calibrated using 25 % O_2/Ar and 5 % H_2/Ar certified gas standards introduced at known flow rates. Raw mass-spectrometer signals were processed with a custom Mathematica routine provided by the Sandia LSFR team: a stationary wavelet transform for denoising, subtraction of a polynomial fit to a user-selected baseline region, and a linear-regression calibration factor converting the ion signals to mole fractions and then, following the procedure of ref. 13, to molar release rates normalized per mole of perovskite atoms; per-cycle O_2 and H_2 amounts were obtained by integrating over user-selected cycle bounds. Each composition was cycled four times; reported $\Delta\delta$ values are means over cycles 2–4 from integrated O_2 release, with cycle 1 excluded to avoid preconditioning effects (see Experimental validation).

Author contributions

Manish Kumar: Data curation, Formal analysis, Investigation, Methodology, Software, Validation, Visualization, Writing – original draft, Writing – review & editing; Natalia Ali: Data curation, Formal analysis, Investigation, Methodology, Validation, Visualization, Writing – original draft, Writing – review & editing; Matthew D. Witman: Data curation, Formal analysis, Funding acquisition, Investigation, Resources, Software, Validation, Visualization, Writing – original draft, Writing – review & editing; Shang Zhai: Funding acquisition, Writing – review & editing; James E. Miller: Formal analysis, Methodology, Supervision, Validation, Writing – original draft, Writing – review & editing; Ivan Ermanoski: Formal analysis, Methodology, Supervision, Validation, Writing – original draft, Writing – review & editing; Ellen B. Stechel: Conceptualization, Formal analysis, Funding acquisition, Methodology, Project administration, Resources, Supervision, Validation, Writing – original draft, Writing – review & editing; Robert B. Wexler: Conceptualization, Formal analysis, Funding acquisition, Methodology, Project administration, Resources, Software, Supervision, Validation, Visualization, Writing – original draft, Writing – review & editing.

Conflicts of interest

There are no conflicts to declare.

Data availability

The processed data supporting this article, including the first-principles oxygen-vacancy formation energies, the crystal-feature-model and defect graph neural network predictions, and the experimental thermogravimetric, stagnation-flow-reactor, and powder X-ray diffraction measurements, together with the scripts that generate all figures, are available at `https://github.com/wexlergroup/cctm-screening`; that repository will be archived at Zenodo, with the DOI provided prior to publication. The underlying VASP density-functional-theory inputs and outputs are deposited in the NOMAD repository (DOI: `10.17172/nomad.6d7e-hvb1`).

Acknowledgements

This material is based upon work supported by the U.S. Department of Energy's Office of Energy Efficiency and Renewable Energy (EERE) under the Fuel Cell Technologies Office (FCTO) under Award Number DE-EE0010733. The authors gratefully acknowledge research support from the HydroGEN Advanced Water Splitting Materials Consortium, established as part of the Energy Materials Network under the U.S. Department of Energy, Office of Energy Efficiency and Renewable Energy, Fuel Cell Technologies Office, under Award Number DE-EE0010733. Specifically, the authors would like to recognize the following HydroGEN experts and capabilities: Anthony McDaniel, Ethan Hecht, Keith King, and Maria Syrigou at the Sandia National Laboratories Laser Heated Stagnation Flow Reactor for Characterizing Redox Chemistry, for their assistance with LSFR access, training, and loading of samples into the reactor for remote experimentation. The authors gratefully acknowledge the use of XRD facilities within the Eyring Materials Center at Arizona State University, supported in part by NNCI-ECCS-1542160. A portion of the research was performed using computational resources sponsored by the Department of Energy's Office of Energy Efficiency and Renewable Energy and located at the National Renewable Energy Laboratory. The views and opinions of the authors expressed herein do not necessarily state or reflect those of the United States Government or any agency thereof. Neither the United States Government nor any agency thereof, nor any of their employees, makes any warranty, expressed or implied, or assumes any legal liability or responsibility for the accuracy, completeness, or usefulness of any information, apparatus, product, or process disclosed, or represents that its use would not infringe privately owned rights.

Sandia National Laboratories is a multi-mission laboratory managed and operated by National Technology & Engineering Solutions of Sandia, LLC (NTESS), a wholly owned subsidiary of Honeywell International Inc., for the U.S. Department of Energy's National Nuclear Security Administration (DOE/NNSA) under contract DE-NA0003525. This written work is authored by an employee of NTESS. The employee, not NTESS, owns the right, title and interest in and to the written work and is responsible for its contents. Any subjective views or opinions that might be expressed in the written work do not necessarily represent the views of the U.S. Government. The publisher acknowledges that the U.S. Government retains a non-exclusive, paid-up, irrevocable,

world-wide license to publish or reproduce the published form of this written work or allow others to do so, for U.S. Government purposes. The DOE will provide public access to results of federally sponsored research in accordance with the DOE Public Access Plan.

References

1 J. T. Tran, K. J. Warren, S. A. Wilson, C. L. Muhich, C. B. Musgrave and A. W. Weimer, *WIREs Energy and Environment*, 2024, **13**, e528.

2 R. B. Wexler, E. B. Stechel and E. A. Carter, *Solar Fuels*, Wiley, 1st edn, 2023, pp. 1–63.

3 W. C. Chueh, C. Falter, M. Abbott, D. Scipio, P. Furler, S. M. Haile and A. Steinfeld, *Science*, 2010, **330**, 1797–1801.

4 S. Lany, *Journal of the American Chemical Society*, 2024, jacs.4c02688.

5 R. J. Panlener, R. N. Blumenthal and J. E. Garnier, *Journal of Physics and Chemistry of Solids*, 1975, **36**, 1213–1222.

6 S. S. Naghavi, A. A. Emery, H. A. Hansen, F. Zhou, V. Ozolins and C. Wolverton, *Nature Communications*, 2017, **8**, 285.

7 Z. Ma and J. Martinek, *Journal of Solar Energy Engineering*, 2019, **141**, 021003.

8 V. K. Budama, J. P. Rincon Duarte, M. Roeb and C. Sattler, *Solar Energy*, 2023, **249**, 353–366.

9 W.-H. Cheng, A. De La Calle, H. A. Atwater, E. B. Stechel and C. Xiang, *ACS Energy Letters*, 2021, **6**, 3096–3113.

10 Z. Ma, P. Davenport and G. Saur, *Renewable Energy*, 2022, **190**, 294–308.

11 S. L. Millican, J. M. Clary, C. B. Musgrave and S. Lany, *Chemistry of Materials*, 2022, **34**, 519–528.

12 C. Liu, J. Park, H. A. De Santiago, B. Xu, W. Li, D. Zhang, L. Zhou, Y. Qi, J. Luo and X. Liu, *ACS Catalysis*, 2024, **14**, 14974–15013.

13 A. H. McDaniel, E. C. Miller, D. Arifin, A. Ambrosini, E. N. Coker, R. O'Hayre, W. C. Chueh and J. Tong, *Energy & Environmental Science*, 2013, **6**, 2424.

14 C. Liu, D. Zhang, W. Li, J. A. Trindell, K. A. King, S. R. Bishop, J. D. Sugar, A. H. McDaniel, A. I. Smith, P. A. Salinas, E. N. Coker, A. L. Clauser, M. Velayutham, J. C. Neuefeind, J. Yang, H. A. De Santiago, L. Ma, Y. Wang, Q. Wang, W. Li, Q. Wang, Q. Li, H. Tian, H. N. Ngan Tran, X. Li, B. Robinson, A. M. Deibel, G. Collins, N. A. Thieu, J. Hu, V. V. Khramtsov, J. Luo and X. Liu, *Journal of Materials Chemistry A*, 2023, **12**, 3910–3922.

15 V. Arzumanyan, C. Liu, D. Zhang, W. Li, J. Luo, X. Liu and Y. Qi, *Solid State Ionics*, 2025, **432**, 117067.

16 D. Zhang, J. Park, B. Xu, C. Liu, W. Li, X. Liu, Y. Qi and J. Luo, *Dalton Transactions*, 2023, **52**, 1082–1088.

17 A. L. Fernandes Cauduro, E. Gager, K. A. King, D. McCord, A. H. McDaniel, J. Scheffe, J. C. Nino and F. El Gabaly, *Topics in Catalysis*, 2024, **67**, 900–908.

18 B. Xu, J. Park, D. Zhang, H. A. De Santiago, W. Li, X. Liu, J. Luo, S. Lany and Y. Qi, *Chemistry of Materials*, 2024, **36**, 4990–5001.

19 R. J. Morelock, J. T. Tran, J. A. Trindell, Z. J. L. Bare, A. H. McDaniel, A. W. Weimer and C. B. Musgrave, *Chemistry of Materials*, 2024, **36**, 5331–5342.

20 D. C. McCord, E. J. Gager, X. Wang, T. L. Johnson, J. S. Beachy, K. A. King, S. R. Phillpot, J. C. Nino, A. H. McDaniel and J. R. Scheffe, *The Journal of Physical Chemistry C*, 2024, **128**, 15796–15806.

21 D. C. McCord, C. M. Hill, F. Barbieri, E. J. Gager, J. C. Nino and J. R. Scheffe, *EES Solar*, 2025, **1**, 267–278.

22 H. N. N. Tran, C. Liu, D. Zhang, Q. Li, J. Yang, S. Chen, W. Li, L. Li, Q. Wang, H. A. De Santiago, L. Ma, Y. Wang, G. Collins, J. Luo and X. Liu, *International Journal of Hydrogen Energy*, 2025, **177**, 151577.

23 X. Wang, A. Goyal, P. Zhou, E. Gager, D. McCord, J. C. Nino, J. R. Scheffe, S. Lany and S. R. Phillpot, *The Journal of Physical Chemistry C*, 2023, **127**, 23988–24000.

24 D. Zhang, H. A. De Santiago, B. Xu, C. Liu, J. A. Trindell, W. Li, J. Park, M. A. Rodriguez, E. N. Coker, J. D. Sugar, A. H. McDaniel, S. Lany, L. Ma, Y. Wang, G. Collins, H. Tian, W. Li, Y. Qi, X. Liu and J. Luo, *Chemistry of Materials*, 2023, **35**, 1901–1915.

25 D. C. McCord, E. J. Gager, K. Lee, A. H. McDaniel, J. C. Nino and J. R. Scheffe, *Journal of Solar Energy Engineering*, 2023, **146**, 021005.

26 D. R. Barcellos, M. D. Sanders, J. Tong, A. H. McDaniel and R. P. O'Hayre, *Energy & Environmental Science*, 2018, **11**, 3256–3265.

27 S. Roychoudhury, S. Shulda, A. Goyal, R. T. Bell, S. Sainio, N. A. Strange, J. E. Park, E. N. Coker, S. Lany, D. S. Ginley and D. Prendergast, *Chemistry of Materials*, 2023, **35**, 1935–1947.

28 J. Perry, L. Molina, A. De La Calle, R. Peño, T. W. Jones, M. V. Ganduglia-Pirovano, S. Jiménez-Fernández, S. W. Donne, J. M. Coronado and A. Bayon, *npj Computational Materials*, 2025, **11**, 247.

29 G. Sai Gautam, E. B. Stechel and E. A. Carter, *Chemistry of Materials*, 2020, **32**, 9964–9982.

30 R. B. Wexler, G. Sai Gautam, R. T. Bell, S. Shulda, N. A. Strange, J. A. Trindell, J. D. Sugar, E. Nygren, S. Sainio, A. H. McDaniel, D. Ginley, E. A. Carter and E. B. Stechel, *Energy & Environmental Science*, 2023, **16**, 2550–2560.

31 A. A. Emery, J. E. Saal, S. Kirklin, V. I. Hegde and C. Wolverton, *Chemistry of Materials*, 2016, **28**, 5621–5634.

32 Y. Kumagai, N. Tsunoda, A. Takahashi and F. Oba, *Physical Review Materials*, 2021, **5**, 123803.

33 B. Baldassarri, J. He, A. Gopakumar, S. Griesemer, A. J. A. Salgado-Casanova, T.-C. Liu, S. B. Torrisi and C. Wolverton, *Chemistry of Materials*, 2023, **35**, 10619–10634.

34 R. B. Wexler, G. S. Gautam, E. B. Stechel and E. A. Carter, *Journal of the American Chemical Society*, 2021, **143**, 13212–13227.

35 M. D. Witman, A. Goyal, T. Ogitsu, A. H. McDaniel and S. Lany, *Nature Computational Science*, 2023, **3**, 675–686.

36 M. D. Witman, R. E. Jones, A. J. E. Rowberg and S. Lany, *Journal of Physics: Energy*, 2026, **8**, 015001.

37 J. Dukić, S. Bošković and B. Matović, *Ceramics International*, 2009, **35**, 787–790.

38 J. M. Naik, B. Bulfin, C. A. Triana, D. C. Stoian and G. R. Patzke, *ACS Applied Materials & Interfaces*, 2023, **15**, 806–817.

39 W. Sun, S. T. Dacek, S. P. Ong, G. Hautier, A. Jain, W. D. Richards, A. C. Gamst, K. A. Persson and G. Ceder, *Science Advances*, 2016, **2**, e1600225.

40 A. M. Deml, A. M. Holder, R. P. O'Hayre, C. B. Musgrave and V. Stevanović, *The Journal of Physical Chemistry Letters*, 2015, **6**, 1948–1953.

41 J. M. Rondinelli and N. A. Spaldin, *Advanced Materials*, 2011, **23**, 3363–3381.

42 J. M. Rondinelli, S. J. May and J. W. Freeland, *MRS Bulletin*, 2012, **37**, 261–270.

43 Y. Bai, Y. Xia, H. Li, L. Han, Z. Wang, X. Wu, S. Lv, X. Liu and J. Meng, *The Journal of Physical Chemistry C*, 2012, **116**, 16841–16847.

44 E.-L. Rautama, T.-S. Chan, R.-S. Liu, J.-M. Chen, H. Yamauchi and M. Karppinen, *Journal of Solid State Chemistry*, 2005, **179**, 111–116.

45 J. M. Cowley, *Physical Review*, 1950, **77**, 669–675.

46 J. M. Cowley, *Physical Review*, 1965, **138**, A1384–A1389.

47 D. Gehringer, M. Friák and D. Holec, *Computer Physics Communications*, 2023, **286**, 108664.

48 X. Qian, J. He, E. Mastronardo, B. Baldassarri, C. Wolverton and S. M. Haile, *Chemistry of Materials*, 2020, **32**, 9335–9346.

49 X. Qian, J. He, E. Mastronardo, B. Baldassarri, W. Yuan, C. Wolverton and S. M. Haile, *Matter*, 2021, **4**, 688–708.

50 T. Das, J. D. Nicholas and Y. Qi, *Journal of Materials Chemistry A*, 2017, **5**, 4493–4506.

51 B. Baldassarri, J. He and C. Wolverton, *Physical Review Materials*, 2024, **8**, 055407.

52 S. Kumar, P. Ghosh and G. S. Gautam, *First-principles investigation of Sr-Ce-M-O perovskites for solar thermochemical water splitting*, 2025, `http://arxiv.org/abs/2509.00779`.

53 A. Zunger, S.-H. Wei, L. G. Ferreira and J. E. Bernard, *Physical Review Letters*, 1990, **65**, 353–356.

54 A. van de Walle, P. Tiwary, M. de Jong, D. L. Olmsted, M. Asta, A. Dick, D. Shin, Y. Wang, L. Q. Chen and Z. K. Liu, *Calphad*, 2013, **42**, 13–18.

55 M. Ångqvist, W. A. Muñoz, J. M. Rahm, E. Fransson, C. Durniak, P. Rozyczko, T. H. Rod and P. Erhart, *Advanced Theory and Simulations*, 2019, **2**, 1900015.

56 P. Virtanen, R. Gommers, T. E. Oliphant, M. Haberland, T. Reddy, D. Cournapeau, E. Burovski, P. Peterson, W. Weckesser, J. Bright, S. J. van der Walt, M. Brett, J. Wilson, K. J. Millman, N. Mayorov, A. R. J. Nelson, E. Jones, R. Kern, E. Larson, C. J. Carey, İ. Polat, Y. Feng, E. W. Moore, J. VanderPlas, D. Laxalde, J. Perktold, R. Cimrman, I. Henriksen, E. A. Quintero, C. R. Harris, A. M. Archibald, A. H. Ribeiro, F. Pedregosa, P. van Mulbregt and SciPy 1.0 Contributors, *Nature Methods*, 2020, **17**, 261–272.

57 G. Sai Gautam and E. A. Carter, *Physical Review Materials*, 2018, **2**, 095401.

58 O. Y. Long, G. Sai Gautam and E. A. Carter, *Physical Review Materials*, 2020, **4**, 045401.

59 B. Baldassarri, J. He, X. Qian, E. Mastronardo, S. Griesemer, S. M. Haile and C. Wolverton, *Physical Review Materials*, 2023, **7**, 065403.

60 Y.-L. Lee, J. Kleis, J. Rossmeisl and D. Morgan, *Physical Review B*, 2009, **80**, 224101.

61 G. Henkelman, A. Arnaldsson and H. Jónsson, *Computational Materials Science*, 2006, **36**, 354–360.

62 W. Tang, E. Sanville and G. Henkelman, *Journal of Physics: Condensed Matter*, 2009, **21**, 084204.

63 S. P. Ong, L. Wang, B. Kang and G. Ceder, *Chemistry of Materials*, 2008, **20**, 1798–1807.

64 S. P. Ong, A. Jain, G. Hautier, B. Kang and G. Ceder, *Electrochemistry Communications*, 2010, **12**, 427–430.

65 S. P. Ong, W. D. Richards, A. Jain, G. Hautier, M. Kocher, S. Cholia, D. Gunter, V. L. Chevrier, K. A. Persson and G. Ceder, *Computational Materials Science*, 2013, **68**, 314–319.

66 C. Freysoldt, B. Grabowski, T. Hickel, J. Neugebauer, G. Kresse, A. Janotti and C. G. Van de Walle, *Reviews of Modern Physics*, 2014, **86**, 253–305.

67 J. Chase, Malcolm W., *NIST-JANAF Thermochemical Tables*, American Institute of Physics, Woodbury, NY, 4th edn, 1998.

68 J. Sun, A. Ruzsinszky and J. P. Perdew, *Phys. Rev. Lett.*, 2015, **115**, 036402.

69 P. J. Huber, *The Annals of Mathematical Statistics*, 1964, **35**, 73–101.

70 P. J. Huber and E. M. Ronchetti, *Robust Statistics*, Wiley, 1st edn, 2009.

71 M. P. Pechini, *Method of preparing lead and alkaline earth titanates and niobates and coating method using the same to form a capacitor*, 1967, US Patent 3,330,697.

72 N. Ali *et al.*, manuscript in preparation.

73 J. R. Scheffe, M. D. Allendorf, E. N. Coker, B. W. Jacobs, A. H. McDaniel and A. W. Weimer, *Chemistry of Materials*, 2011, **23**, 2030–2038.

74 D. Arifin, V. J. Aston, X. Liang, A. H. McDaniel and A. W. Weimer, *Energy & Environmental Science*, 2012, **5**, 9438.

75 J. R. Scheffe, A. H. McDaniel, M. D. Allendorf and A. W. Weimer, *Energy & Environmental Science*, 2013, **6**, 963.

Supplementary Information for "Local B-site chemistry controls oxygen-vacancy energetics in Ca–Ce–Ti–Mn perovskites for thermochemical hydrogen production"

Manish Kumar,[‡] Natalia Ali,[‡] Matthew D. Witman, Shang Zhai, James E. Miller, Ivan Ermanoski, Ellen B. Stechel, and Robert B. Wexler

S1 Magnetic moments and oxidation-state assignments

Calculated oxidation-state assignments in CCTM perovskites were made from site-resolved magnetic moments obtained by integrating the spin density within projector augmented wave (PAW) spheres, as reported in the Vienna ab initio simulation package (VASP) `OUTCAR` file. Fig. S1 shows the distribution of site-resolved $|\mu|$ by element across all six CCTM compositions. Ca, Ti, and O sites carry negligible moments (median $|\mu| < 0.05\,\mu_B$), consistent with Ca^{2+}, Ti^{4+}, and O^{2-}. Ce moments fall almost entirely within a narrow window of 0.45–0.85 μ_B (Ce^{3+}-like), with a single site at 0.13 μ_B assigned to Ce^{4+}-like $4f^0$ occupation. Mn moments span 3.0–4.1 μ_B and are assigned to oxidation states using ionic crystal-field expectations:[1, 2] $|\mu_{Mn}| < 3.4\,\mu_B$ for Mn^{4+} ($3d^3$, $S = 3/2$), 3.4–4.0 μ_B for Mn^{3+} ($3d^4$, $S = 2$), and >4.0 μ_B for Mn^{2+} ($3d^5$, $S = 5/2$). Some overlap between adjacent ranges is expected from local distortions and Mn–O covalency, which modulate the spin density within PAW spheres. These assignments are consistent with the projected density of states reported in Section S2.

Of the 138 Ce sites across the six bulk supercells, 137 are labeled Ce^{3+} and 1 Ce^{4+} using a cutoff at $|\mu_{Ce}| = 0.4\,\mu_B$, placed in the empty interval between the lone low-moment site and the main cluster. This binary labeling is coarse-grained, and the Ce^{3+}/Ce^{4+} labels classify calculated moments rather than measured oxidation states. Ce sites classified as Ce^{3+}-like have calculated PAW-sphere spin moments of 0.45–0.85 μ_B, compared with 0.94 μ_B for fully localized Ce^{3+} in hexagonal Ce_2O_3 within the same strongly constrained and appropriately normed functional with Hubbard U corrections (SCAN+U) framework;[3] these moments indicate fractional $4f$ occupation, consistent with partial Ce $4f$–O $2p$ hybridization on the A sublattice. No oxidation state was measured for the compositions synthesized in this work. The single low-moment site occurs in CCTM2112 ($Ca_{0.67}Ce_{0.33}Ti_{0.33}Mn_{0.67}O_3$), the supercell referenced in the main text. Table S1 gives the per-composition breakdown.

We checked that these assignments are insensitive to the choice of real-space partition by comparing PAW-sphere moments to Bader moments, obtained with the Henkelman-group grid-based `bader` code[4, 5] using the self-consistent valence charge density as the charge reference for basin assignment and integrating the spin density over the resulting atomic basins. Across the 2160 sites in the six bulk supercells, the mean absolute deviation (MAD) is 0.014 μ_B; across the 32 310

[‡]These authors contributed equally to this work.

matched sites in the 90 defective supercells used in Section S3 the MAD for vacancy-induced moment changes $\Delta|\mu|$ is $0.005\,\mu_B$. The Ce classification is unchanged, so it does not depend on the partition, although neither partition measures a formal oxidation state; 7 of the 276 Mn sites, all within $0.04\,\mu_B$ of the $3.4\,\mu_B$ Mn^{4+}/Mn^{3+} cutoff, reclassify from Mn^{3+} to Mn^{4+} under Bader partitioning (shifting the bulk counts from 84, 191 and 1 to 91, 184 and 1), consistent with the near-boundary overlap noted above.

The Ce^{3+}-like state does not depend on the initial magnetic moments. Our earlier calculations on CCTM2112[1] initialized the Ce and Mn moments at 0.6 and $4.0\,\mu_B$, whereas the present calculations used 1.0 and $5.0\,\mu_B$. Two single-point SCAN+U calculations of the relaxed CCTM2112 supercell, started from the earlier and the present initial moments, converge to the same electronic state: every site moment agrees within $0.007\,\mu_B$, and their total energies, both computed with VASP 6.5.1, differ by 0.5 meV per 360-atom supercell. Because this test keeps the geometry fixed, it does not exclude a Ce^{4+}-like state with its own relaxed structure.

Table S2 summarizes the vacancy-induced changes in the local moments by element for all six compositions (response to oxygen-vacancy formation in the 90 defective supercells). In every composition, the changes occur on Ce and Mn, with smaller induced moments on O, whereas individual Ti and Ca moments change by less than $0.05\,\mu_B$; Ce and Mn are therefore the redox-active cations throughout the composition range studied. Within a supercell, individual Mn sites can change in opposite directions, some consistent with reduction and others with oxidation, so the summed site-level magnitudes of the Mn changes (1.1–$2.7\,\mu_B$) exceed the net Mn change, as also found in the earlier study;[1] for Ce, the summed site-level magnitudes (0.86–$1.03\,\mu_B$) are closer to the net change. These moment changes are computational indicators of the redox response rather than a measure of electron transfer.

Table S1: Per-composition counts of Ce^{3+} and Ce^{4+} sites in the bulk 360-atom SQS supercells, assigned from PAW-sphere magnetic moments using $|\mu_{Ce}| > 0.4\,\mu_B$ as the threshold for $4f^1$ occupation. The single low-moment site occurs in CCTM2112.

Composition	X_{Ce}	X_{Mn}	N_{Ce}	$N_{Ce^{3+}}$	$N_{Ce^{4+}}$
$Ca_{0.75}Ce_{0.25}Ti_{0.50}Mn_{0.50}O_3$	0.25	0.50	18	18	0
$Ca_{0.71}Ce_{0.29}Ti_{0.42}Mn_{0.58}O_3$	0.29	0.58	21	21	0
$Ca_{0.67}Ce_{0.33}Ti_{0.33}Mn_{0.67}O_3$	0.33	0.67	24	23	1
$Ca_{0.63}Ce_{0.37}Ti_{0.25}Mn_{0.75}O_3$	0.37	0.75	27	27	0
$Ca_{0.67}Ce_{0.33}Ti_{0.42}Mn_{0.58}O_3$	0.33	0.58	24	24	0
$Ca_{0.67}Ce_{0.33}Ti_{0.25}Mn_{0.75}O_3$	0.33	0.75	24	24	0

Table S2: Vacancy-induced changes in the PAW-sphere moment magnitudes by element, averaged over the 15 oxygen vacancies of each composition (μ_B per vacancy). Net: signed change in $|\mu|$ summed over all sites of the element. Summed: sum of the site-level magnitudes $|\Delta|\mu||$ over all sites of the element. Ti and Ca changes are below $0.05\,\mu_B$ at every site and are omitted.

			Ce		Mn		O
Composition	X_{Ce}	X_{Mn}	Net	Summed	Net	Summed	Summed
$Ca_{0.75}Ce_{0.25}Ti_{0.50}Mn_{0.50}O_3$	0.25	0.50	0.94	1.00	0.67	1.10	0.44
$Ca_{0.71}Ce_{0.29}Ti_{0.42}Mn_{0.58}O_3$	0.29	0.58	0.76	0.88	0.70	1.36	0.55
$Ca_{0.67}Ce_{0.33}Ti_{0.33}Mn_{0.67}O_3$	0.33	0.67	0.70	0.89	0.65	2.15	0.70
$Ca_{0.63}Ce_{0.37}Ti_{0.25}Mn_{0.75}O_3$	0.37	0.75	0.55	0.86	1.13	2.04	0.68
$Ca_{0.67}Ce_{0.33}Ti_{0.42}Mn_{0.58}O_3$	0.33	0.58	0.86	1.03	0.52	1.91	0.71
$Ca_{0.67}Ce_{0.33}Ti_{0.25}Mn_{0.75}O_3$	0.33	0.75	0.70	1.02	0.57	2.66	0.87

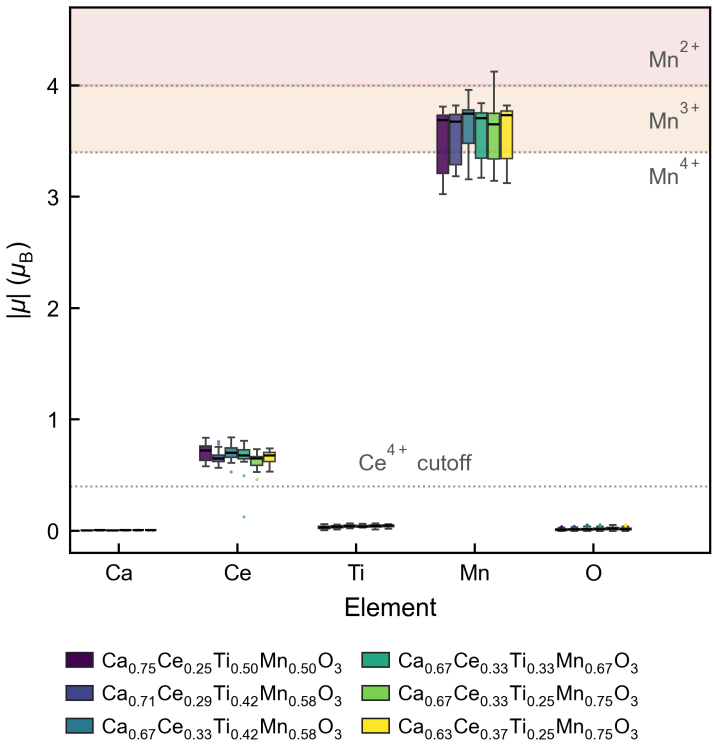


Figure S1: Distribution of site-resolved $|\mu|$ from PAW-sphere integration, by element, across all six bulk 360-atom special quasirandom structure (SQS) supercells. Boxes span the interquartile range (IQR), and whiskers extend to 1.5× IQR. Shaded bands indicate the Mn assignment ranges (Mn^{3+}, Mn^{2+}); the dotted lines mark the $Mn^{4+}/Mn^{3+}/Mn^{2+}$ cutoffs at 3.4 μ_B and 4.0 μ_B and the Ce^{4+}/Ce^{3+} cutoff at 0.4 μ_B.

S2 Density of states and metallic character

Fig. S2a shows the spin-resolved total density of states for the six bulk CCTM compositions, computed at the supercell zone center on the 360-atom Γ-relaxed cells. The pattern is consistent across the composition range: in each composition, the spin-up channel carries a finite DOS at the Fermi level (0.1–0.2 states eV^{-1} $atom^{-1}$), while the spin-down channel is gapped around E_F. The compositional spread of the total DOS is small (Fig. S2a, $\pm1\sigma$ envelope), indicating that the metallic character is a family-wide feature rather than a property of any single composition. At the SCAN+U level adopted here, CCTM perovskites are therefore metallic and fully spin-polarized at E_F across the composition range studied.

Fig. S2b decomposes the DOS of $Ca_{0.75}Ce_{0.25}Ti_{0.50}Mn_{0.50}O_3$ by element and orbital character. The states crossing E_F are dominated by partially filled Ce $4f$ orbitals, with a smaller Mn $3d$ contribution. The valence band is principally O $2p$ with hybridized Mn $3d$ character (−7 to −2 eV); the conduction band (1–4 eV) carries both Mn $3d$ and unoccupied Ce $4f$ weight. That the Ce $4f$ band spans E_F rather than localizing fully below it reflects the bandwidth of the dense Ce sublattice relative to $U_{Ce} = 2.0$ eV,[3] and is consistent with the delocalized-reduction picture: electrons released on vacancy formation are accommodated across multiple partially filled Ce $4f$ sites rather than via discrete $Ce^{4+} \rightarrow Ce^{3+}$ transitions.

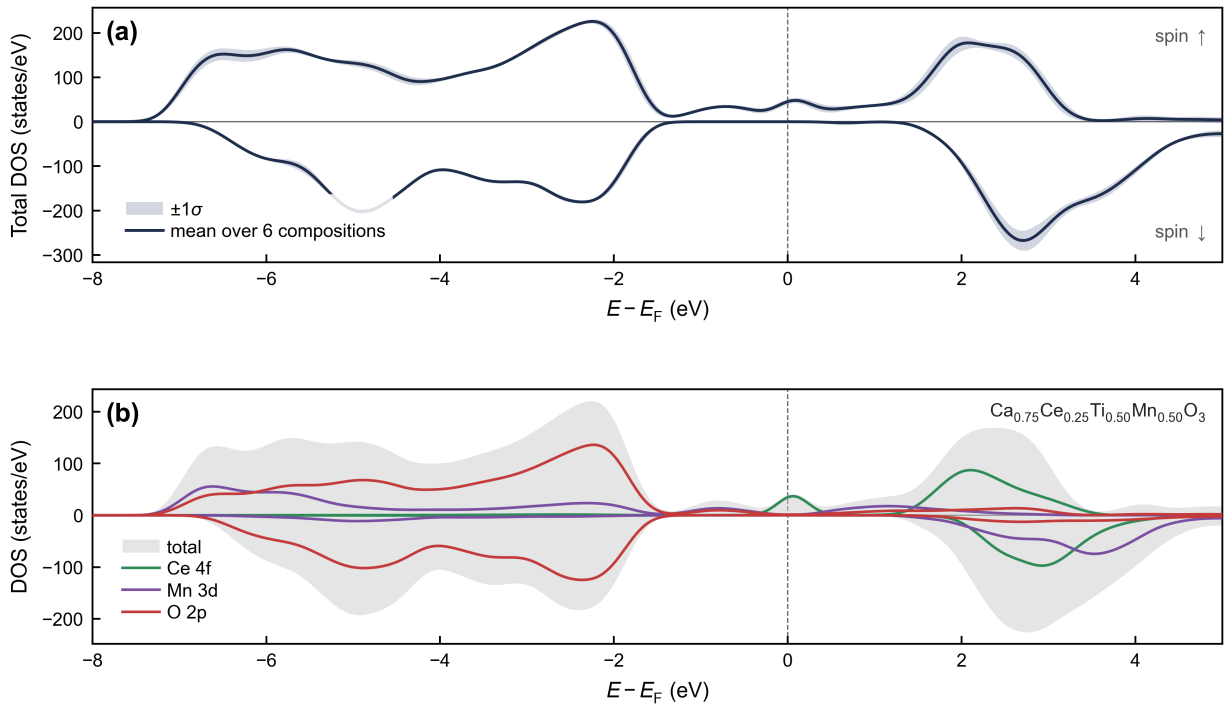


Figure S2: Spin-resolved density of states of CCTM perovskites at the Γ point. (a) Total DOS averaged across the six bulk 360-atom SQS supercells (dark line: mean; shaded envelope: $\pm 1\sigma$ across compositions). (b) Element- and orbital-resolved decomposition for $Ca_{0.75}Ce_{0.25}Ti_{0.50}Mn_{0.50}O_3$: total DOS (gray fill), Ce $4f$ (green), Mn $3d$ (purple), and O $2p$ (red). The dashed vertical line in each panel marks the Fermi level.

S3 Crystal-feature model parity

The crystal-feature model (CFM) introduced in the main text approximates the oxygen-vacancy formation energy E_v at each symmetry-distinct site as a linear combination of two physically motivated descriptors of the local environment: the mean crystal bond dissociation energy $\langle E_\mathrm{b} \rangle$ and the mean crystal reduction potential $\langle V_\mathrm{r} \rangle$ of the six first-nearest-neighbor cations (four A-site, two B-site) of the vacant oxygen. The per-cation crystal bond dissociation energies and crystal reduction potentials follow the definitions of ref. 6 (eqn (2) and (5) therein); see Section S11 for the values used here and for the averaging convention. We fit the regression

$$E_\mathrm{v} = \beta_\mathrm{b} \langle E_\mathrm{b} \rangle + \beta_\mathrm{r} \langle V_\mathrm{r} \rangle + c \tag{S1}$$

on the full density functional theory (DFT) dataset of 90 symmetry-distinct oxygen sites across the six CCTM compositions of main-text Table 1. Ref. 6 additionally included the per-composition energy above the convex hull E_hull as a descriptor in their parent model. We omit it here because our composition set contains only six unique E_hull values across the narrow range 18–39 meV atom^{-1}, which is insufficient to constrain β_hull (see the descriptor-subset comparison at the end of this section).

We evaluate eqn (S1) under two complementary cross-validation schemes. Random 50 %/50 % train–test splits, repeated 1000 times following the protocol of ref. 6, measure prediction accuracy at held-out sites within the sampled composition space. Leave-one-group-out (LOGO) cross-validation

with composition as the group, in which each of the six compositions is held out in turn and the model is fit on the remaining five, measures generalization to compositions outside the training set; this is the relevant criterion for subsequent screening of the per-cycle oxygen-exchange capacity $\Delta\delta$ across composition space.[7] For each split, we fit a Huber regressor on the training partition and compute the mean absolute error (MAE) on the held-out partition; for random splits, we report the mean and standard deviation of MAE across the 1000 splits, and for LOGO, the mean and standard deviation across the six folds. Reported coefficients are obtained from a single Huber fit (the scikit-learn `HuberRegressor`[8] with its default settings, $\epsilon = 1.35$ and $\alpha = 10^{-4}$) to the full 90-site dataset; 95 % confidence intervals are obtained by bootstrap resampling of sites with replacement (2000 resamples). An ordinary least squares fit on the same data yields coefficients within these bootstrap confidence intervals and MAE within 0.001 eV.

Fig. S3 shows parity plots of SCAN+U E_v against the CFM-predicted E_v for two parameterizations of the model: one in which the per-cation $E_{\mathrm{b},n}$ and $V_{\mathrm{r},n}$ are taken from the SCAN+U binary-oxide calculations of ref. 6 (Fig. S3a), and one in which they are taken from the compilation of experimental binary-oxide thermochemistry in the same work (Fig. S3b). Both parameterizations yield MAE = 0.175(15) eV across the 1000 random splits, and MAE = 0.174(42) eV under LOGO. The random-split and LOGO MAEs are equal within the across-fold standard deviation, indicating that the model generalizes to held-out compositions essentially as well as to held-out sites within sampled compositions, supporting the use of the CFM for composition-space screening of $\Delta\delta$. The MAE is small relative to the spread of E_v across the dataset (2.15 eV, main-text Fig. 3), corresponding to a relative error of approximately 8 % of the E_v range.

The identical MAEs of the two parameterizations, despite slightly different fitted β_b and β_r values, arise because the SCAN+U and experimental $E_{\mathrm{b},n}$ and $V_{\mathrm{r},n}$ tabulated by ref. 6 agree closely across the cations present in CCTM (MAE of 0.04 eV between SCAN+U and experimental E_b across their perovskite-oxide composition space); any feature-scale difference between the two sources is compensated by a corresponding adjustment in β_b and β_r. The agreement indicates that the CFM prediction is insensitive to whether the per-cation features are supplied from SCAN+U calculations or from experimental thermochemistry, within their binary-oxide reference set.

The fitted coefficient signs match the extended Born–Haber picture of vacancy formation, applicable to either parameterization. A positive β_b yields higher predicted E_v at sites whose nearest-neighbor cations have stronger crystal bonds (larger E_b), because vacancy formation breaks four A–O and two B–O bonds in proportion to their crystal bond dissociation energies. A negative β_r yields lower predicted E_v at sites whose nearest-neighbor cations are more easily reduced (less negative V_r), because the two electrons left behind by oxygen removal localize on the cation sublattice at lower energy cost when the surrounding cations are more reducible.

Table S3 reports the LOGO MAE for the CFM under selected subsets of the candidate descriptors $\{\langle E_\mathrm{b}\rangle,\ \langle V_\mathrm{r}\rangle,\ E_\mathrm{hull}\ \}$ and supports the choice of $\langle E_\mathrm{b}\rangle$ and $\langle V_\mathrm{r}\rangle$ alone in eqn (S1). Removing E_hull from the parent three-descriptor model changes the LOGO MAE from 0.175(47) eV to 0.174(42) eV, a difference well inside the across-fold standard deviation. Refitting the three-descriptor model on the full 90-site dataset yields $\beta_\mathrm{hull} = -4.77$ with a bootstrap 95 % confidence interval of $[-13.13, +3.74]$ that spans zero, consistent with there being only six unique E_hull values across the dataset to constrain it. By contrast, removing $\langle E_\mathrm{b}\rangle$ individually raises the LOGO MAE to 0.25 eV and removing $\langle V_\mathrm{r}\rangle$ raises it to 0.36 eV; E_hull on its own yields a LOGO MAE of 0.50 eV, comparable to the mean absolute deviation of E_v across the dataset (0.49 eV) and therefore no better than predicting the dataset mean for every site.

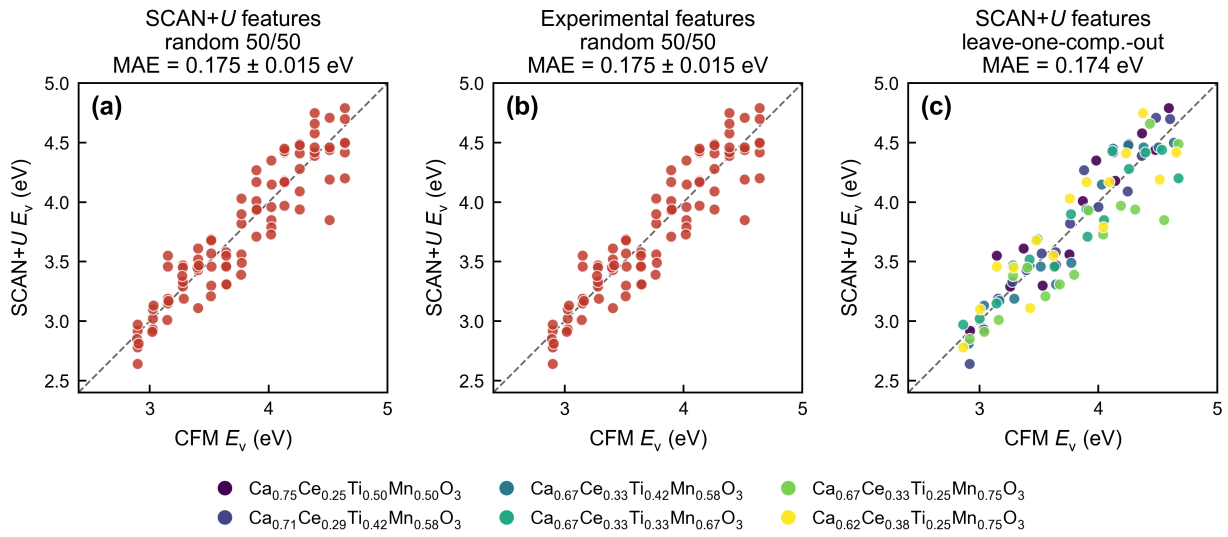


Figure S3: Parity plots comparing SCAN+U oxygen-vacancy formation energies of CCTM perovskites with crystal-feature-model predictions, using per-cation features from (a) the SCAN+U binary-oxide calculations and (b) the compilation of experimental binary-oxide thermochemistry, both reported in ref. 6, each under random 50 %/50 % train–test splits; and (c) the SCAN+U features under leave-one-composition-out cross-validation, with points colored by composition (legend). The dashed line indicates perfect agreement; all three panels share the same axis range to allow direct visual comparison. Panels (a) and (b) yield MAE = 0.175(15) eV across 1000 random 50 %/50 % train–test splits; panel (c) yields MAE = 0.174(42) eV under leave-one-composition-out cross-validation. Fitted coefficients (full-data Huber fit; bootstrap 95 % confidence intervals in brackets), SCAN+U features: $\beta_{\mathrm{b}} = +2.00$ $[+1.78, +2.23]$, $\beta_{\mathrm{r}} = -1.34$ $[-1.64, -1.04]$, $c = -4.26$ $[-4.94, -3.58]$. Experimental features: $\beta_{\mathrm{b}} = +1.52$ $[+1.31, +1.74]$, $\beta_{\mathrm{r}} = -1.57$ $[-1.92, -1.22]$, $c = -3.85$ $[-4.52, -3.16]$.

S4 Vacancy–vacancy electrostatic upper bound

The statistical-mechanical model of main-text Methods (formalized in Section S7) treats oxygen vacancies as independent point defects: configurational entropy is taken in its ideal-solution form, and the per-vacancy reduction enthalpy is approximated by the dilute-limit DFT value E_{v}. This functional form is justified, beyond its agreement with experimental $\delta(T, P_{\mathrm{O_2}})$, when the vacancy–vacancy interaction V_{vv} at experimentally accessed vacancy densities is small compared with the thermal energy $k_{\mathrm{B}}T$ under reduction conditions. We bound V_{vv} from above using Thomas–Fermi screening in the metallic host (Section S2).

In the metallic host, two notional $+2e$ point charges (an upper bound on any residual local charge a neutral vacancy might carry, corresponding to the formal Kröger–Vink $V_{\mathrm{O}}^{\bullet\bullet}$ defect) interact via a Yukawa-screened potential

$$V_{\mathrm{vv}}(r) = \frac{(2e)^2}{4\pi\varepsilon_0\, r}\, \exp(-r/\lambda_{\mathrm{TF}})\,, \qquad \lambda_{\mathrm{TF}} = \sqrt{\frac{\varepsilon_0}{e^2\, g(E_{\mathrm{F}})}}, \tag{S2}$$

where $g(E_{\mathrm{F}})$ is the Fermi-level density of states per unit volume. Using the smoothed mean total DOS at E_{F} across the six bulk compositions (Fig. S2a, $\sim$45 states eV^{-1} per 360-atom supercell

Table S3: Performance of the crystal-feature model under selected subsets of the candidate descriptors $\{\langle E_\mathrm{b}\rangle, \langle V_\mathrm{r}\rangle, E_\mathrm{hull}\}$, evaluated by leave-one-composition-out cross-validation (LOGO MAE reported as mean ± standard deviation across the six folds). $\langle E_\mathrm{b}\rangle$ and $\langle V_\mathrm{r}\rangle$ each contribute substantively to the prediction; including E_hull does not change the LOGO MAE within fold-to-fold variance, and E_hull is therefore excluded from eqn (S1). [a] Descriptor set used in eqn (S1).

Descriptors	LOGO MAE (eV)
$\langle E_\mathrm{b}\rangle$, $\langle V_\mathrm{r}\rangle$, E_hull	0.175(47)
$\langle E_\mathrm{b}\rangle$, $\langle V_\mathrm{r}\rangle$ [a]	0.174(42)
$\langle E_\mathrm{b}\rangle$ only	0.253(28)
$\langle V_\mathrm{r}\rangle$ only	0.364(59)
E_hull only	0.496(44)

at $V_\mathrm{cell} \approx 4080\,\text{Å}^3$) gives $\lambda_\mathrm{TF} \approx 0.71\,\text{Å}$. Reducing $g(E_\mathrm{F})$ to $\sim$20 states eV^{-1} per supercell as a conservative-low sensitivity case extends λ_TF to 1.06 Å.

The vacancy–vacancy separation relevant to the statistical-mechanical model is set by the experimental oxygen off-stoichiometry δ. Across the reduction conditions accessed by thermogravimetric analysis (TGA; Section S6, peak temperature $\sim$1623 K), δ_red spans approximately 0.03–0.07. For vacancies randomly distributed on the oxygen sublattice at density $n_\mathrm{v} = 3\delta/V_\mathrm{fu}$ ($V_\mathrm{fu} \approx 56.6\,\text{Å}^3$), the Wigner–Seitz radius is

$$r_\mathrm{WS} = \left(\frac{3}{4\pi n_\mathrm{v}}\right)^{1/3} = \left(\frac{V_\mathrm{fu}}{4\pi\delta}\right)^{1/3}, \tag{S3}$$

giving $r_\mathrm{WS} \approx 5.3\,\text{Å}$ at $\delta_\mathrm{red} = 0.03$ and 4.0 Å at $\delta_\mathrm{red} = 0.07$. At these separations, eqn (S2) yields $V_\mathrm{vv} \approx 6$–50 meV at the family-mean λ_TF (Fig. S4, blue curve). Comparison with $k_\mathrm{B}T \approx 140$ meV at the reduction temperature places the worst-case Yukawa interaction a factor of approximately 3–20 below the thermal scale across the experimentally accessed range, supporting the noninteracting-vacancy approximation of the statistical-mechanical model. The conservative-low λ_TF sensitivity (orange curve) lies on both sides of $k_\mathrm{B}T$ over the same r range; even here, the interaction remains within a factor of a few of $k_\mathrm{B}T$, and the corrections discussed next reduce it further.

Three considerations indicate that this estimate overstates the actual interaction. First, the $(2e)^2$ prefactor assumes the full Kröger–Vink charge state; the neutral V_O^0 defects treated in the formation-energy framework carry zero formal charge in the metallic host, so the actual leading-order monopole–monopole interaction vanishes and the residual contribution is dominated by higher multipoles and elastic terms, both of which are typically meV-scale at the relevant separations. Second, Thomas–Fermi captures the leading-order metallic screening but neglects the wavevector dependence of the dielectric function (Lindhard / random-phase-approximation corrections) and the local depletion of $g(E_\mathrm{F})$ in the immediate neighborhood of the vacancy, both of which further suppress V_vv at the short distances relevant here. Third, a random distribution of vacancies is an upper bound on the mean-field interaction: any short-range configurational repulsion between like-charged defects would increase r_WS relative to the random value used in eqn (S3). Each of these corrections reduces V_vv further below the Yukawa estimate plotted in Fig. S4.

These bounds, together with the empirical agreement between the statistical-mechanical model and TGA $\delta(T, P_{\mathrm{O}_2})$ isotherms, provide a physical justification for the ideal-solution functional form of the model under experimentally accessed reduction conditions. At higher δ than experimentally probed (e.g., $\delta \gtrsim 0.10$, where $r_\mathrm{WS} < 3.6\,\text{Å}$ and V_vv approaches $k_\mathrm{B}T$ even at the family-mean λ_TF), interactions become nonnegligible and a more elaborate treatment (a cluster expansion, a

Bragg–Williams model, or Wagner-type defect chemistry) would be required.

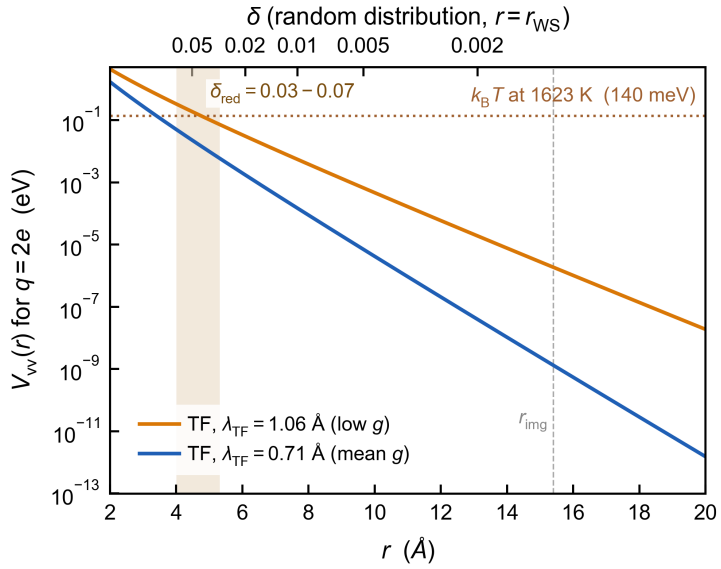


Figure S4: Thomas–Fermi screened vacancy–vacancy electrostatic interaction $V_{\mathrm{vv}}(r)$ (eqn (S2)) for a hypothetical $(2e)^2$ point-charge pair, at the family-mean $g(E_{\mathrm{F}})$ from Fig. S2a (blue, $\lambda_{\mathrm{TF}} = 0.71$ Å) and at a conservative-low $g(E_{\mathrm{F}})$ (orange, $\lambda_{\mathrm{TF}} = 1.06$ Å). Shaded vertical band: range of Wigner–Seitz radii (eqn (S3)) for the reduction-side oxygen off-stoichiometry $\delta_{\mathrm{red}} \approx 0.03$–$0.07$ accessed by TGA (Section S6). Top axis: corresponding δ at $r = r_{\mathrm{WS}}$. Dotted horizontal line: thermal energy $k_{\mathrm{B}}T$ at the TGA reduction temperature (1623 K). Light dashed vertical line: vacancy–vacancy periodic-image separation in the $(3 \times 3 \times 2)$ SQS supercells, $r_{\mathrm{img}} \approx 15.4$ Å, at which the screened interaction falls to $\sim$1 neV, indicating that the screened electrostatic contribution of periodic images to single-vacancy E_{v} is negligible.

S5 Powder X-ray diffraction

We characterized the phase purity of the three CCTM compositions synthesized for the TGA and laser-heated stagnation flow reactor (LSFR) experiments by powder X-ray diffraction; full chemical formulas appear in main-text Table 3, and synthesis and acquisition conditions are described in main-text Methods. Fig. S5 stacks the three experimental patterns with a calculated reference pattern for CCTM2112. All three patterns reproduce the peak positions and relative intensities of the calculated orthorhombic perovskite reference, with no $CeO_2(111)$ reflection at $2\theta = 28.55°$[1] (dashed vertical line) and no additional reflections attributable to secondary phases. No crystalline secondary phase was detected in any of the three samples, which are therefore majority single-phase orthorhombic perovskites. Laboratory XRD does not exclude nanocrystalline or amorphous CeO_2, whose reflections would be broadened into the background.

The calculated reference was generated from the same 360-atom $3 \times 3 \times 2$ SQS supercell of CCTM2112 used in the DFT calculations (main-text Methods) with the `XRDCalculator` module of PYMATGEN[9] using Cu Kα_1 radiation (1.540 56 Å); the calculated line pattern was convolved with a Gaussian of FWHM 0.10° for visual comparison with the experimental traces.

Fig. S6 compares the patterns of two samples recovered after cycling with their as-synthesized

patterns: $Ca_{0.71}Ce_{0.29}Ti_{0.42}Mn_{0.58}O_3$ ($X_{Ce} = 0.29$) after the four LSFR cycles of main-text Fig. 6, and CCTM2112 after 20 TGA cycles (Protocols A, B, and C, followed by further cycling). Neither post-cycling pattern shows secondary phases, decomposition, or structural changes relative to the corresponding as-synthesized pattern.

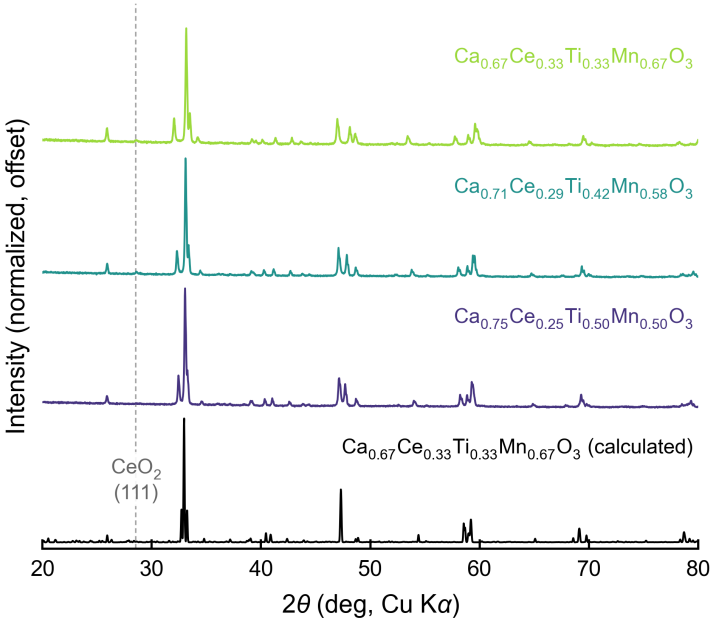


Figure S5: Powder X-ray diffraction patterns of the three CCTM compositions synthesized for the TGA and LSFR experiments (top three traces, ordered top-to-bottom by descending Mn content) and a calculated reference pattern for CCTM2112 (bottom trace). The dashed vertical line at $2\theta = 28.55°$ marks the position of the $CeO_2(111)$ reflection, the strongest reflection of CeO_2 and the expected indicator of cerium exsolution, observed as a minor CeO_2 second phase in a prior refinement of a higher-Ce CCTM composition.[1] The calculated reference was generated from the 360-atom $3\times3\times2$ SQS supercell of CCTM2112 using the `XRDCalculator` module of PYMATGEN with Cu Kα_1 radiation (1.540 56 Å), convolved with a Gaussian profile of FWHM 0.10°; experimental patterns were collected with Cu Kα radiation (see main-text Methods).

S6 Thermogravimetric analysis

Fig. S7 shows the temperature and oxygen-content cycling traces obtained on the three CCTM compositions during Protocol B cycling. Protocol B uses a two-step reduction at 1350 °C (1 h) followed by 1300 °C (0.5 h) under flowing Ar, and reoxidation at 900 °C (0.5 h) under 20 % O_2/Ar; full Protocol A and Protocol C conditions are described in main-text Methods. Acquisition was performed on a NETZSCH STA 449 F3 Jupiter thermogravimetric analyzer with 80 mg of CCTM powder loaded in a calcia-stabilized zirconia crucible and heated at 10 °C min^{-1} to the reduction temperature.

As in main-text Methods, cycle 1 is a preconditioning (break-in) cycle and is excluded from the reported averages, because the as-synthesized material is more oxidized than the steady-state cycled state. The per-cycle oxygen-exchange capacity is approximately constant across cycles for all three compositions, with a cycle-to-cycle standard deviation no larger than 0.0013 (CCTM2112) over

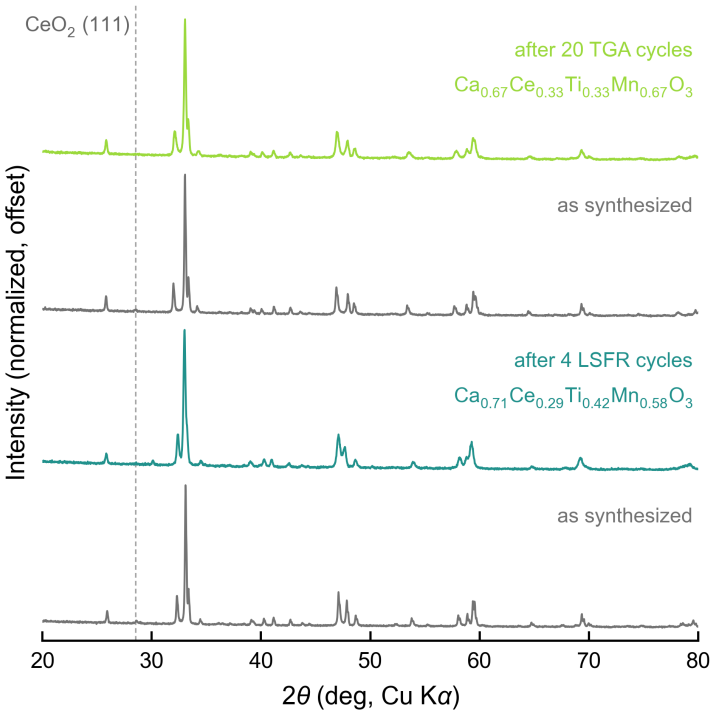


Figure S6: Powder X-ray diffraction patterns of $Ca_{0.71}Ce_{0.29}Ti_{0.42}Mn_{0.58}O_3$ ($X_{Ce} = 0.29$) as synthesized and after the four LSFR cycles of main-text Fig. 6 (bottom two traces), and of CCTM2112 ($Ca_{0.67}Ce_{0.33}Ti_{0.33}Mn_{0.67}O_3$) as synthesized and after 20 TGA cycles (Protocols A, B, and C, followed by further cycling; top two traces). Each trace is normalized to its maximum and offset vertically; experimental patterns were collected with Cu Kα radiation. The dashed vertical line at $2\theta = 28.55°$ marks the position of the CeO_2(111) reflection.

cycles 2–5. Throughout this section the end-of-step δ values are referenced to the as-loaded (initial) state, so they report the change in oxygen content relative to that state, not the absolute deficiency in $ABO_{3-\delta}$; δ therefore decreases (becomes negative) as the sample loses oxygen on reduction. The traces plotted in Fig. S7 show the same referenced δ shifted so that the most-reduced point of each run is zero. This referenced δ is distinct from the per-cycle oxygen-exchange capacity $\Delta\delta$ reported in main-text Table 3, which is a positive quantity. For CCTM2112 (bottom panel), the end-of-reduction δ becomes progressively more negative across cycles (from -0.038 in cycle 1 to -0.084 in cycle 5) and the end-of-reoxidation δ drifts correspondingly, indicating that the 0.5 h reoxidation dwell at 900 °C under 20 % O_2/Ar is insufficient to re-establish the same oxidized state cycle-to-cycle; the per-cycle excursion is essentially unaffected by this drift. $Ca_{0.75}Ce_{0.25}Ti_{0.50}Mn_{0.50}O_3$ and $Ca_{0.71}Ce_{0.29}Ti_{0.42}Mn_{0.58}O_3$ (top and middle panels) show negligible cycle-to-cycle drift in both the reduction and reoxidation endpoints, consistent with steady-state cycling under Protocol B. $\Delta\delta$ values reported in main-text Table 3 are averaged over cycles 2–5.

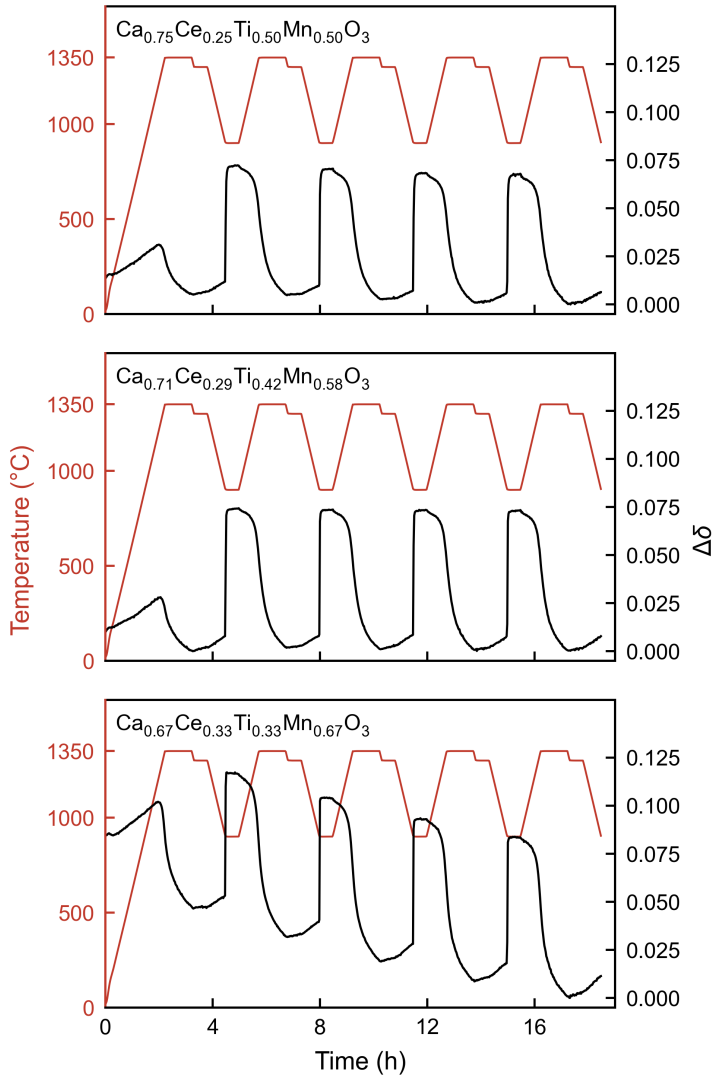


Figure S7: Thermogravimetric Protocol B cycling traces for the three CCTM compositions, ordered top-to-bottom by ascending Mn content. Each panel shows temperature (red, left axis) and the change in oxygen content, plotted relative to the most-reduced state of the run (black, right axis; the per-cycle excursion of this trace equals $\Delta\delta$), over five reduction–reoxidation cycles; reduction holds at 1350 °C for 1 h followed by 1300 °C for 0.5 h under flowing Ar, and reoxidation holds at 900 °C for 0.5 h under 20 % O_2/Ar. $\Delta\delta$ was computed from the measured mass change as described in main-text Methods. Cycle-to-cycle drift in the end-of-reduction and end-of-reoxidation δ values is most pronounced for CCTM2112 (bottom panel); $\Delta\delta$ values reported in main-text Table 3 average over cycles 2–5.

S7 Finite-temperature thermodynamic formalism

This section provides the formal link between the 0 K DFT vacancy formation energy E_{v} (tabulated throughout the main text) and the equilibrium oxygen deficiency $\delta(T, P)$ used to predict cycle-level performance. Four components are needed: (i) the free-energy decomposition that allows a temperature-independent E_{v} to appear in a finite-temperature occupation expression (Section S7.1); (ii) the equilibrium occupation derived from a two-state lattice-gas model (Section S7.2); (iii) the gas-phase chemical-potential references that supply μ_{O}under reduction and water-splitting conditions (Section S7.3); and (iv) a numerical example carrying the evaluation from E_{v} through to $\Delta\delta$ for CCTM2112 (Section S7.4).

S7.1 From the 0 K DFT energy to the finite-temperature free energy

Removing one oxygen from a stoichiometric supercell to a gas-phase O_2 reservoir is written

$$\mathrm{ABO_3\,(pristine)} \rightarrow \mathrm{ABO_{3-3/}}_{N_{\mathrm{O}}}\,\mathrm{(defective)} + \tfrac{1}{2}\,\mathrm{O_2(g)}, \tag{S4}$$

for a supercell containing N_{O} oxygen atoms. The associated free-energy change, neglecting vibrational contributions from the solid (harmonic-phonon calculations across oxides show the solid-state vibrational entropy of vacancy formation to be the smaller contribution to the total reduction entropy, with a high-temperature dependence that largely counterbalances that of the O_2 gas entropy[10]), is

$$\Delta G_{\mathrm{v}}(T, P_{\mathrm{O_2}}) \approx E_{\mathrm{def}}^{\mathrm{DFT}} - E_{\mathrm{prist}}^{\mathrm{DFT}} + \tfrac{1}{2}\,\mu_{\mathrm{O_2}}(T, P_{\mathrm{O_2}}), \tag{S5}$$

where $E_{\mathrm{def}}^{\mathrm{DFT}}$ and $E_{\mathrm{prist}}^{\mathrm{DFT}}$ are the DFT total energies of the defective and pristine supercells. Splitting the gas-phase chemical potential into a DFT reference and an ideal-gas thermal contribution,

$$\mu_{\mathrm{O_2}}(T, P_{\mathrm{O_2}}) = E_{\mathrm{O_2}}^{\mathrm{DFT}} + \Delta\mu_{\mathrm{O_2}}(T, P_{\mathrm{O_2}}), \tag{S6}$$

where $E_{\mathrm{O_2}}^{\mathrm{DFT}}$ is the SCAN total energy of an isolated O_2 molecule computed with the same settings as the solids and

$$\Delta\mu_{\mathrm{O_2}}(T, P_{\mathrm{O_2}}) = G^{\circ}_{\mathrm{O_2}}(T) + k_{\mathrm{B}}T\ln\!\big(P_{\mathrm{O_2}}/P^{\circ}\big), \tag{S7}$$

with $G^{\circ}_{\mathrm{O_2}}(T)$ the standard Gibbs energy at temperature T from the tables of Section S7.3 and $P^{\circ} = 1\,\mathrm{bar}$. Substituting eqn (S6) and (S7) into eqn (S5) and grouping DFT terms gives

$$\Delta G_{\mathrm{v}}(T, P_{\mathrm{O_2}}) = E_{\mathrm{v}} + \mu_{\mathrm{O}}(T, P_{\mathrm{O_2}}), \tag{S8}$$

with

$$E_{\mathrm{v}} = E_{\mathrm{def}}^{\mathrm{DFT}} - E_{\mathrm{prist}}^{\mathrm{DFT}} + \tfrac{1}{2}\,E_{\mathrm{O_2}}^{\mathrm{DFT}}, \tag{S9}$$

the temperature-independent 0 K DFT vacancy formation energy (the quantity tabulated throughout the main text) and

$$\mu_{\mathrm{O}}(T, P_{\mathrm{O_2}}) \equiv \tfrac{1}{2}\,\Delta\mu_{\mathrm{O_2}}(T, P_{\mathrm{O_2}}), \tag{S10}$$

the per-atom shift of the oxygen chemical potential relative to the $E_{\mathrm{O_2}}^{\mathrm{DFT}}/2$ reference. Eqn (S10) is the quantity denoted μ_{O}in main-text Methods eqn (6): the $E_{\mathrm{O_2}}^{\mathrm{DFT}}/2$ reference is implicit there because it cancels with the corresponding term in E_{v} (eqn (S9)). Positive E_{v} corresponds to endothermic vacancy formation at 0 K; more negative μ_{O}(lower $P_{\mathrm{O_2}}$or higher T) lowers ΔG_{v} and favors vacancy formation, consistent with the expectation that reducing atmospheres promote oxide reduction.

S7.2 Equilibrium occupation from a two-state lattice-gas model

With each oxygen site treated as a distinguishable position on the lattice in equilibrium with the gas-phase reservoir at chemical potential μ_{O}, every site has two states: occupied by O^{2-} (formation energy 0, particle number $n_{\mathrm{O}} = 1$) or vacant (formation energy E_{v}, $n_{\mathrm{O}} = 0$), as in standard ideal-solution defect-equilibrium treatments.[11] The single-site grand partition function is then

$$\Xi = \exp(\mu_{\mathrm{O}}/k_{\mathrm{B}}T) + \exp(-E_{\mathrm{v}}/k_{\mathrm{B}}T)\,, \tag{S11}$$

and the probability that the site is vacant is

$$n(E_{\mathrm{v}}, T, \mu_{\mathrm{O}}) = \frac{\exp(-E_{\mathrm{v}}/k_{\mathrm{B}}T)}{\Xi} = \frac{1}{1 + \exp[(E_{\mathrm{v}} + \mu_{\mathrm{O}})/k_{\mathrm{B}}T]}, \tag{S12}$$

the quantity appearing in main-text Methods eqn (4).

The CCTM perovskites are configurationally disordered, and distinct local nearest-neighbor environments $\mathbf{x} = (x_{\mathrm{Ce}}, x_{\mathrm{Mn}})$ carry distinct E_{v} values. Each oxygen has four A-site and two B-site nearest-neighbor cations, so x_{Ce} takes values 0, 1/4, 1/2, 3/4 and 1 and x_{Mn} takes values 0, 1/2 and 1, yielding 15 symmetry-distinct local environments. Under an ideal-solution approximation for the bulk cation distribution, the probability of finding a given $\mathbf{x}$ at bulk composition $\mathbf{X} = (X_{\mathrm{Ce}}, X_{\mathrm{Mn}})$ is binomial,

$$P(\mathbf{x} \mid \mathbf{X}) = \binom{4}{4x_{\mathrm{Ce}}} X_{\mathrm{Ce}}^{4x_{\mathrm{Ce}}} (1 - X_{\mathrm{Ce}})^{4(1-x_{\mathrm{Ce}})} \binom{2}{2x_{\mathrm{Mn}}} X_{\mathrm{Mn}}^{2x_{\mathrm{Mn}}} (1 - X_{\mathrm{Mn}})^{2(1-x_{\mathrm{Mn}})}, \tag{S13}$$

where the factors of 4 and 2 are the A- and B-site coordination numbers of each oxygen in the perovskite structure. The bulk oxygen deficiency is the binomial-weighted average of eqn (S12) over the 15 environments,

$$\delta(T, \mu_{\mathrm{O}}) = 3 \sum_{\mathbf{x}} P(\mathbf{x} \mid \mathbf{X})\, n(E_{\mathrm{v}}(\mathbf{x}, \mathbf{X}), T, \mu_{\mathrm{O}})\,, \tag{S14}$$

where the prefactor of 3 accounts for the three oxygen atoms per ABO_3 formula unit. This expression relies on the independent-site (dilute-vacancy) approximation, whose validity at experimentally accessed δ is discussed in Section S4, and on the ideal-solution approximation for the bulk cation distribution.[12] The SCAN+U and CFM entries of main-text Table 3 are obtained by evaluating eqn (S14) directly using DFT- and CFM-predicted per-environment E_{v}, respectively. The dGNN entries (main-text Fig. 5b and Table 3) are obtained by evaluating the corresponding average empirically over the 216 oxygen sites of an SQS supercell (Section S8.3); the two estimators agree to within $\pm 4\,\%$ on $\Delta\delta$ across the six DFT compositions of main-text Table 1, well inside the spread between the CFM and dGNN.

S7.3 Gas-phase chemical-potential references

Thermochemical functions for O_2(g), H_2(g), and H_2O(g) were obtained from the NIST Chemistry WebBook,[13] which tabulates Shomate-equation coefficients derived from the NIST-JANAF Thermochemical Tables.[14] The Shomate parameterization expresses the standard heat capacity, enthalpy, and entropy as polynomials in $t = T/1000\,\mathrm{K}$:

$$C_P^{\circ}(T) = A + Bt + Ct^2 + Dt^3 + E/t^2, \tag{S15}$$

$$H^{\circ}(T) - H^{\circ}(298.15\,\mathrm{K}) = At + \tfrac{B}{2}t^2 + \tfrac{C}{3}t^3 + \tfrac{D}{4}t^4 - E/t + F - H, \tag{S16}$$

$$S^{\circ}(T) = A\ln t + Bt + \tfrac{C}{2}t^2 + \tfrac{D}{3}t^3 - E/(2t^2) + G, \tag{S17}$$

where C_P° and S° are in $\mathrm{J\,mol^{-1}\,K^{-1}}$ and H° in $\mathrm{kJ\,mol^{-1}}$. The standard Gibbs energy is then

$$G_i^\circ(T) = \Delta_\mathrm{f} H_i^\circ(298.15\,\mathrm{K}) + \big[H_i^\circ(T) - H_i^\circ(298.15\,\mathrm{K})\big] - T\,S_i^\circ(T), \tag{S18}$$

with $\Delta_\mathrm{f} H_i^\circ(298.15\,\mathrm{K}) = 0$ for O_2 and H_2 in their reference states and $\Delta_\mathrm{f} H_{\mathrm{H_2O}}^\circ(298.15\,\mathrm{K}) = -241.826\,\mathrm{kJ\,mol^{-1}}$ for $H_2O\,(g)$. The chemical potential of species i at partial pressure P_i follows from

$$\mu_i(T, P_i) = G_i^\circ(T) + k_\mathrm{B} T \ln\!\big(P_i/P^\circ\big). \tag{S19}$$

The expressions for $\mu_\mathrm{O}$under the reduction and water-splitting limits (main-text Methods eqn (6) and (8)) follow from eqn (S19) applied to the appropriate species labels. Table S4 lists the coefficient sets used; the temperature ranges shown bracket the reduction (1123–1623 K) and water-splitting (1123 K) conditions of this work, and the corresponding coefficient sets are the only ones evaluated.

Table S4: Shomate-equation coefficients for the gas-phase species used in this work, taken from the NIST Chemistry WebBook (NIST Standard Reference Database 69).[a] The coefficient sets shown are the only ones evaluated; low-temperature sets are not used at the cycling conditions of this work.

Species	T range (K)	A	B	C	D	E	F	G	H
O_2	700–2000	30.032	8.773	−3.988	0.788	−0.742	−11.325	236.166	0
H_2	1000–2500	18.563	12.257	−2.860	0.268	1.978	−1.147	156.288	0
H_2O	500–1700	30.092	6.833	6.793	−2.534	0.082	−250.881	223.397	−241.826

[a] Units of the resulting quantities: C_P° in $\mathrm{J\,mol^{-1}\,K^{-1}}$, H° in $\mathrm{kJ\,mol^{-1}}$, S° in $\mathrm{J\,mol^{-1}\,K^{-1}}$.

S7.4 Worked example: CCTM2112 under cycling conditions

To illustrate the complete procedure, we evaluate eqn (S12) and (S14) for CCTM2112 at the screening conditions of main-text Methods.

Reduction. At $T_\mathrm{red} = 1623.15\,\mathrm{K}$ (1350 °C) and $P_{\mathrm{O_2}} = 1 \times 10^{-4}\,\mathrm{bar}$, evaluation of eqn (S16)–(S18) with the O_2 row of Table S4 gives $G_{\mathrm{O_2}}^\circ(T_\mathrm{red}) = -378.5\,\mathrm{kJ\,mol^{-1}}$ (equivalently, −3.92 eV per molecule). Inserting this into eqn (S19) and halving per eqn (S10),

$$\mu_\mathrm{O}(T_\mathrm{red}, P_{\mathrm{O_2}}) = \tfrac{1}{2}\big[G_{\mathrm{O_2}}^\circ(T_\mathrm{red}) + k_\mathrm{B} T_\mathrm{red} \ln(P_{\mathrm{O_2}}/P^\circ)\big] = -2.61\,\mathrm{eV}.$$

Water splitting. At $T_\mathrm{ox} = 1123.15\,\mathrm{K}$ (850 °C) and $P_{\mathrm{H_2O}}/P_{\mathrm{H_2}} = 1000$, the same procedure applied to H_2O and H_2 gives $G_{\mathrm{H_2O}}^\circ(T_\mathrm{ox}) = -4.95\,\mathrm{eV}$ and $G_{\mathrm{H_2}}^\circ(T_\mathrm{ox}) = -1.72\,\mathrm{eV}$ per molecule, so that

$$\mu_\mathrm{O}(T_\mathrm{ox}, P_{\mathrm{H_2O}}, P_{\mathrm{H_2}}) = G_{\mathrm{H_2O}}^\circ(T_\mathrm{ox}) - G_{\mathrm{H_2}}^\circ(T_\mathrm{ox}) + k_\mathrm{B} T_\mathrm{ox} \ln(P_{\mathrm{H_2O}}/P_{\mathrm{H_2}}) = -2.56\,\mathrm{eV}.$$

Occupation and oxygen-exchange capacity. CCTM2112 has $X_\mathrm{Ce} = 1/3$ and $X_\mathrm{Mn} = 2/3$. Substituting into eqn (S13) gives the binomial probability of each of the 15 local environments, dominated by $(x_\mathrm{Ce}, x_\mathrm{Mn}) \in \{(1/4, 1/2),\ (1/4, 1),\ (1/2, 1/2),\ (1/2, 1)\}$ (i.e., one to two Ce among the four A-site neighbors and one to two Mn among the two B-site neighbors) with $P \in [0.13, 0.20]$ each. Across the 15 sites, the SCAN+U E_v values span 2.97–4.44 eV with binomial-weighted mean $\langle E_\mathrm{v}\rangle = 3.49\,\mathrm{eV}$ (Table S5). Substituting $\langle E_\mathrm{v}\rangle$ into eqn (S12) at the two conditions above gives $n_\mathrm{red} = 1.8 \times 10^{-3}$ and $n_\mathrm{ox} = 6.6 \times 10^{-5}$, hence $\delta_\mathrm{red} \approx 5.4 \times 10^{-3}$, $\delta_\mathrm{ox} \approx 2.0 \times 10^{-4}$, and $\Delta\delta \approx 5.2 \times 10^{-3}$. This single-mean estimate systematically underestimates $\Delta\delta$ because $n(E_\mathrm{v})$ is strongly nonlinear in E_v and the site distribution is broad: environments with $E_\mathrm{v} < \langle E_\mathrm{v}\rangle$ contribute disproportionately. Evaluating eqn (S14) over the binomial-weighted environment distribution instead gives $\delta_\mathrm{red} = 0.052$,

$\delta_{ox} = 8.7 \times 10^{-3}$, and $\Delta\delta = 0.044$, an order of magnitude larger than the single-mean estimate. This is the value reported in the SCAN+U column of main-text Table 3 for CCTM2112; the CFM and dGNN entries follow the related estimators described after eqn (S14).

Table S5: The 15 symmetry-distinct oxygen first-nearest-neighbor environments of CCTM2112 ($X_{Ce} = 1/3$, $X_{Mn} = 2/3$): local A-site Ce fraction x_{Ce}, local B-site Mn fraction x_{Mn}, binomial environment probability $P(\mathbf{x} \mid \mathbf{X})$ from eqn (S13), and the representative-site SCAN+U oxygen-vacancy formation energy E_v. The binomial-weighted mean is $\langle E_v \rangle = 3.49\,\text{eV}$; these are the inputs to the worked example.

x_{Ce}	x_{Mn}	$P(\mathbf{x} \mid \mathbf{X})$	E_v (eV)
0	0	0.022	4.43
0	1/2	0.088	3.69
0	1	0.088	2.97
1/4	0	0.044	4.28
1/4	1/2	0.176	3.46
1/4	1	0.176	3.02
1/2	0	0.033	4.42
1/2	1/2	0.132	3.90
1/2	1	0.132	3.15
3/4	0	0.011	4.44
3/4	1/2	0.044	3.71
3/4	1	0.044	3.47
1	0	0.001	4.20
1	1/2	0.005	3.85
1	1	0.005	3.52

S8 Defect graph neural network model

The defect graph neural network (dGNN) provides a complementary, data-driven counterpart to the linear crystal-feature model of Section S3: it uses the same SCAN+U vacancy formation energies but learns the structure–composition–E_v map without a prescribed functional form, so nonlinear contributions that lie outside the linear form of eqn (S1) can be captured empirically. This section documents the architecture, training and inference protocol, and validation against SCAN+U used to generate the screening predictions of main-text Fig. 5b and the dGNN entries of main-text Table 3.

S8.1 Architecture and training protocol

The dGNN follows the architecture of Witman et al.,[15] a crystal graph convolutional neural network (CGCNN)[16] adapted for site-resolved defect-property prediction. The model takes a relaxed defect-free host structure and the index of a single crystallographic site as input, and outputs the relaxed vacancy formation energy at that site, without ever constructing or relaxing a defective supercell. Atomic-site nodes are initialized with one-hot encodings of nine elemental properties (Mendeleev number, atomic weight, melting temperature, covalent radius, electronegativity, ground-state volume per atom, ground-state band gap, ground-state magnetic moment, and space group number) concatenated with a one-hot encoding of the site oxidation state inferred from the host DFT calculation. Edges are initialized via a radial-basis-function expansion of interatomic distances within a cutoff radius. After $T = 2$ CGCNN convolution steps, the post-convolution

feature vector at the site to be vacated is concatenated with global host descriptors (band gap, effective electron mass, and formation enthalpy of the pristine host) and passed through a single fully connected layer to produce a scalar E_v. The model contains ∼2000 learnable parameters in total; the convolution function, complete node and edge featurizations, and node-level pooling step are specified in Witman et al.[15] For the disordered CCTM SQS supercells, the site oxidation states required as input features are inferred from the SCAN+U-computed local magnetic moments under the constraint of overall charge neutrality, following the convention of Witman et al.[15] This assignment shares the physical basis of the analysis in Section S1 but is carried out within the dGNN featurization of Witman et al., rather than with the explicit moment cutoffs tabulated there.

Training uses K-fold cross-validation with $K = 10$, following Witman et al.[15] The training set is partitioned into K disjoint folds; for each fold, an independent model is trained, with 10 % of the remaining training data held out as a within-fold validation set for early stopping based on the mean absolute error (MAE). At inference, all K models predict E_v for a given input structure; the ensemble mean is reported as the prediction and the ensemble standard deviation as a heuristic uncertainty estimate, used both to flag high-uncertainty individual predictions and to define the upper- and lower-bound envelopes on the screening surface of main-text Fig. 5b. The loss, optimizer, learning rate, batch size, and maximum number of epochs follow Witman et al.,[15] whose architecture and training are implemented in the open-source `cgcnndefect` PyTorch code (`https://github.com/mwitman1/cgcnndefect`); the learning rate was selected to minimize the within-fold validation MAE. The complete training configuration is provided in that code release and in the supplementary information of Douglas et al.[17]

S8.2 Pretraining and fine-tuning datasets

Two datasets are used: a Base dataset for pretraining, and a fine-tuned (FT) dataset that augments the Base data with a fraction of the CCTM vacancy formation energies computed in this work, a transfer-learning strategy for extending defect-property models to chemistries absent from the pretraining set.[18]

The Base dataset is the augmented training set assembled by Douglas et al.,[17] merging (i) the binary and ternary oxide vacancy database of Witman et al.[15] (15 cations across seven crystal systems), (ii) additional quaternary oxides and alloy structures from the validation set of the same study, (iii) the ABO_3 perovskite vacancy database of ref. 6, and (iv) additional binary and ternary oxides newly computed by Douglas et al.[17] The combined Base dataset contains 1859 neutral vacancy formation energies (1047 oxygen and 812 cation) across 253 unique host structures, as compiled in the training-data deposit of Douglas et al.;[17] their Fig. 2a gives the per-cation structure count. The CCTM chemical system lies outside this collection: although all four CCTM cations (Ca, Ce, Ti, Mn) appear individually in the Base data, no four-component Ca–Ce–Ti–Mn–O oxide is present, and the B-site Ti/Mn disorder of CCTM produces nearest-neighbor cation environments that are absent from the Base data, making Base predictions on CCTM a compound-wise extrapolation test.

The FT dataset extends the Base dataset with a randomly drawn 20 % of the 90 CCTM oxygen-vacancy formation energies (18 sites). The remaining 72 CCTM sites are held out from training and serve as the validation set in Section S8.4.

S8.3 Inference and screening

To screen across the (X_{Ce}, X_{Mn}) composition domain, SQS supercells were generated at 100 grid points spanning the same domain as the six DFT compositions of main-text Table 1, using the SQS

construction protocol described in main-text Methods, with three independent realizations at each grid point and a single cell at the four endpoint compositions, which are configurationally ordered. At each grid point the dGNN predicts E_v for every oxygen site of the supercell, yielding an E_v distribution at that composition. The distribution is then averaged via eqn (S14) of Section S7 to produce $\delta(T, \mu_O)$, and the reduction- and oxidation-step occupations are differenced to give $\Delta\delta$ at the cycling conditions of main-text Methods. The 216-site supercell average evaluates eqn (S14) empirically, with the empirical site distribution serving as a finite-supercell approximation to the binomial environment distribution; this approximation is the source of the few-percent spread between the dGNN and SCAN+U estimators noted in Section S7.2. The $\Delta\delta$ surface of main-text Fig. 5b is the result of this calculation evaluated on the 100-point grid; the dGNN entries of main-text Table 3 for off-grid compositions are obtained by linear interpolation of $\Delta\delta(X_{Ce}, X_{Mn})$ between the four nearest grid points.

S8.4 Validation and predicted E_v distributions

The accuracy of the dGNN architecture has been characterized on the Base dataset via nested $(K = 10, L = 10)$-fold cross-validation by Douglas et al.,[17] who report expected MAEs for oxygen-vacancy formation energies of 0.38 eV under structure-wise hold-out (whole structures withheld from training, with their constituent cations still represented elsewhere in the training set) and 0.75 eV under element-wise hold-out (all structures containing a target cation withheld from training). CCTM is out of sample by compound but not by cation, so the relevant generalization regime for Base predictions on CCTM falls between these two bounds, and most closely corresponds to the structure-wise regime.

Fig. S8(a, b) compares dGNN-predicted with SCAN+U E_v for the Base model (evaluated on all 90 CCTM sites) and the FT model (evaluated on the 72-site hold-out, excluding the 18 FT-training sites). Panels (c, d) summarize the per-fold MAE and Pearson R^2 distributions across the $K = 10$ ensemble for each model. The Base model achieves an MAE of 0.29 eV on the full 90-site CCTM set with a mean ensemble standard deviation of 0.44 eV, below the structure-wise hold-out expectation of 0.38 eV and thus consistent with the structure-wise hold-out regime. Fine-tuning reduces the MAE to 0.25 eV on the 72-site hold-out and tightens the mean ensemble standard deviation to 0.16 eV; the FT model overpredicts across the full E_v range (slightly more at high E_v), producing a positive overall bias of 0.14 eV.

Fig. S9 compares the per-site E_v distributions of the fine-tuned dGNN and the CFM across the 100-point composition grid used for screening. The dGNN distribution mean shifts smoothly with composition, but its spread and the position of its lower tail are nonmonotonic across the (X_{Ce}, X_{Mn}) domain; the nonmonotonic ridge along the $CaTiO_3$–$CaMnO_3$ and $CaMnO_3$–$CeMnO_3$ edges of main-text Fig. 5b is traceable to broader dGNN distributions and lower-E_v tails in those regions, both of which raise the count-weighted occupation average of eqn (S14) at fixed mean E_v.

The CFM and dGNN distributions track one another within the CFM's training composition window ($X_{Ce} \in [0.25, 0.375]$, $X_{Mn} \in [0.5, 0.75]$), but the linear CFM compresses predictions into a much narrower range across the broader grid (2.88 eV to 4.65 eV, vs. 1.98 eV to 6.50 eV for the dGNN). The deviation is most pronounced in the $X_{Ce} > X_{Mn}$ half-plane, where the bulk-level Mn^{3+}/Mn^{4+} assignment underlying eqn (S1) extrapolates to formally unphysical values (the bulk-charge-balance Mn oxidation state $n_{Mn} = 4 - X_{Ce}/X_{Mn}$ falls below 3; Section S11). Because the CFM depends on the nearest-neighbor composition alone, its predictions at any one composition take at most 15 discrete E_v values, one per nearest-neighbor cation environment, which appear as the sharp peaks within each subpanel; the dGNN, which incorporates structural context beyond the nearest-neighbor shell of each oxygen site, represents continuous site-to-site variation that the

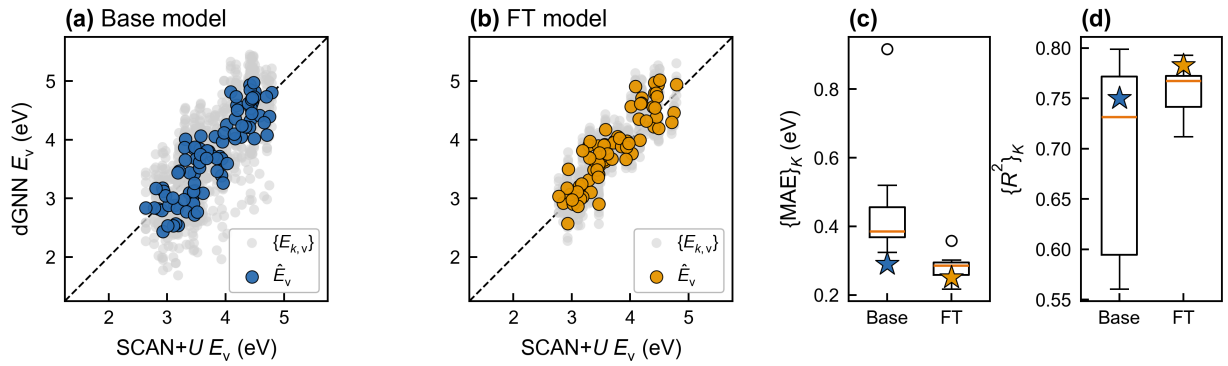


Figure S8: Performance of dGNN E_v predictions on the CCTM compositions. (a) Base model: SCAN+U vs. dGNN-predicted E_v for the 90 CCTM oxygen-vacancy sites; gray points are individual k-fold predictions $\{E_{k,v}\}$, blue points the ensemble mean $\hat{E}_v$. (b) Fine-tuned (FT) model: same, evaluated on the 72-site hold-out (the 18 FT-training sites are excluded), with ensemble means in orange. (c) Per-fold MAE distributions; stars mark the overall ensemble-mean MAE on each model's evaluation set. (d) Per-fold Pearson R^2 distributions; stars mark the ensemble-mean overall R^2. Dashed lines in (a, b) are the identity.

CFM by construction does not.

Fig. S10 condenses the dGNN screening data into line traces. The SQS-averaged mean E_v (panel a) decreases monotonically with X_{Mn} for all X_{Ce}, consistent with Mn being the reducible cation. The SQS standard deviation (panel b) peaks at $X_{Mn} \approx 0.5$, where mixed A-/B-site disorder is maximal; the peak is largest at $X_{Ce} \approx 0.3$–0.5 and shallowest at the $X_{Ce} = 1$ endpoint, tracing out the same broader-distribution regions that drive the ridge in main-text Fig. 5b.

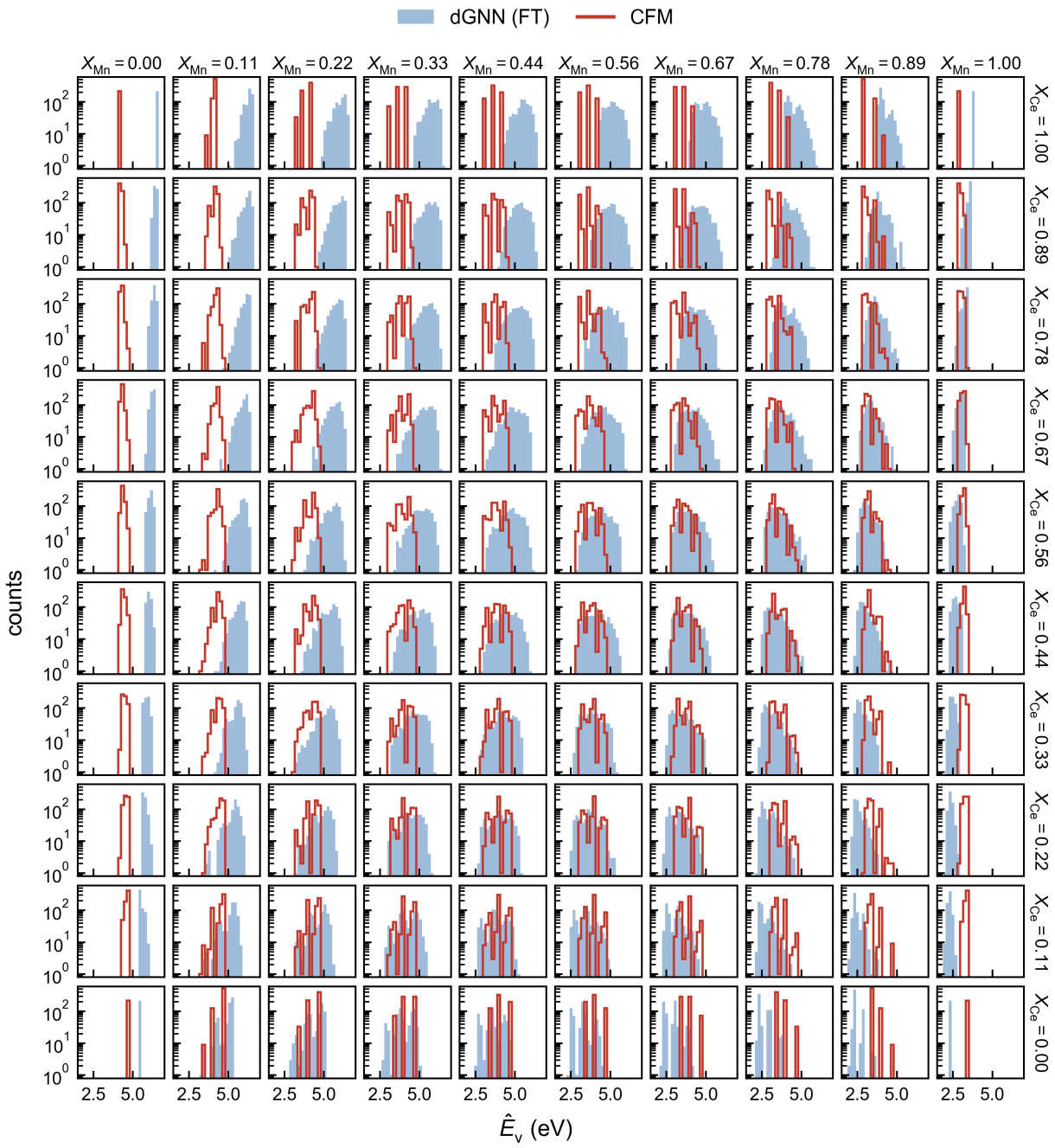


Figure S9: Per-site E_v distributions across the (X_{Ce}, X_{Mn}) screening grid (100 points): fine-tuned dGNN ensemble-mean predictions $\hat{E}_v$ (blue, filled) and CFM predictions (red, outlined). Each subpanel is a log-scale histogram aggregated over all SQS realizations (∼648 oxygen sites at interior grid points, 216 at the four endpoint compositions). CFM evaluation uses the SCAN+U-feature parameterization ($\beta_b = +2.00$, $\beta_r = -1.34$, $c = -4.26$) with fractional Mn assignment from bulk charge balance, $n_{Mn} = 4 - X_{Ce}/X_{Mn}$. The CFM is evaluated on the full grid; in the $X_{Ce} > X_{Mn}$ half-plane n_{Mn} extrapolates below 3 and CFM values there reflect extrapolation by the fitted model outside the charge-balanced regime.

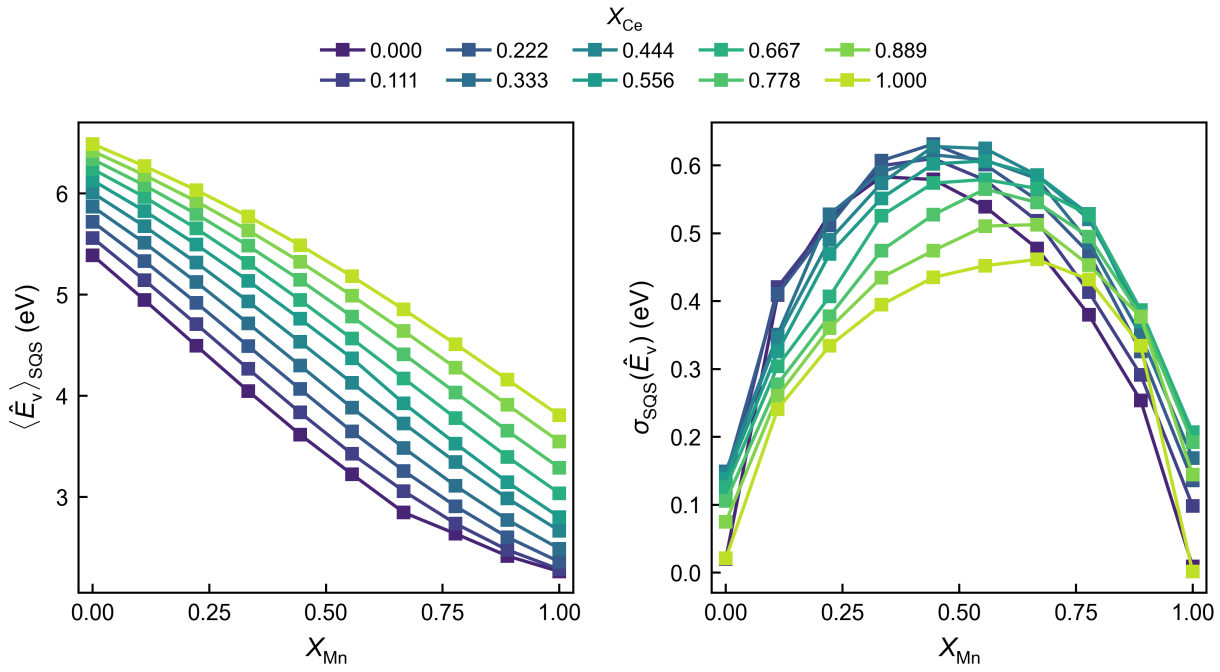


Figure S10: Summary of per-site fine-tuned dGNN E_v distributions across the screening grid. (a) Mean $\langle \hat{E}_v \rangle_{SQS}$ and (b) standard deviation $\sigma_{SQS}(\hat{E}_v)$ vs. X_{Mn}, one line per X_{Ce}.

S9 Configurational sensitivity of bulk energetics under SQS sampling

The default special quasirandom structure (SQS) objective Q in ICET, the package used for SQS generation (main-text Methods), does not constrain which subset of the fifteen symmetry-distinct oxygen first-nearest-neighbor (1NN) environments is realized in a finite supercell. Different stochastic runs at the same composition can therefore produce different environment subsets and yield different total energies, which introduces an uncontrolled variance into bulk quantities such as E_{hull}. The coverage-constrained protocol used in this work (main-text Methods) removes this environment-subset freedom by penalizing supercells that do not realize all fifteen 1NN environments.

For CCTM2112, the coverage-constrained protocol yields $E_{hull} = 33\,\text{meV atom}^{-1}$, within the 33–35 meV atom^{-1} reported for a standard ICET SQS realization of the same composition in ref. 1. The agreement indicates that the configurational sensitivity of E_{hull} at this composition is at most a few meV atom^{-1}, below the resolution of a single-realization comparison. The objective Q attains the same minimum value in the coverage-constrained cells as in standard cells: the objective is degenerate, with multiple equally optimal solutions, and the coverage constraint restricts the optimization to the subset of solutions realizing all fifteen 1NN environments. Coverage is therefore obtained at no cost in the SQS objective Q. Full coverage is also a prerequisite for sampling the complete distribution of local properties, including the lower tail of the site-resolved E_v distribution used throughout this work.

All six compositions in this work were generated under the coverage-constrained protocol, so cross-composition E_{hull} comparisons are internally consistent.

S10 Brillouin-zone sampling convergence

The production calculations sample the Brillouin zone at the supercell zone center (Γ-only), a choice justified by the size of the 360-atom SQS supercells. We tested this choice on the $X_{\mathrm{Ce}} = 0.25$ composition ($Ca_{0.75}Ce_{0.25}Ti_{0.50}Mn_{0.50}O_3$) by performing single-point self-consistent calculations at a Γ-centered $2 \times 2 \times 2$ Monkhorst–Pack mesh on the Γ-relaxed geometries. For the pristine supercell, the denser mesh lowers the total energy by 14 meV per supercell (0.04 meV atom^{-1}), one to two orders of magnitude below conventional convergence thresholds for transition-metal oxides.[6] Fig. S11 overlays the corresponding spin-resolved DOS at the two grid densities; the spectral features track closely, with no qualitative change introduced under denser sampling.

Vacancy formation energies E_{v} are differences of total energies between a defective supercell, the pristine reference, and the oxygen chemical-potential reference (Section S7). The chemical-potential reference is independent of the supercell k-grid, so the k-sampling sensitivity of E_{v} is set by the defective- and pristine-cell total energies alone. We quantified it directly for the highest-frequency vacancy environment in this composition ($x_{\mathrm{Ce}} = 0.25$, $x_{\mathrm{Mn}} = 0.5$), recomputing E_{v} at the $2 \times 2 \times 2$ mesh on the Γ-relaxed geometries: E_{v} decreases from 3.47 eV (Γ-only) to 3.41 eV ($2 \times 2 \times 2$), a shift of 62 meV. Here x_{Ce} and x_{Mn} denote the Ce and Mn fractions among the vacancy's four A-site and two B-site nearest-neighbor cations, in contrast to the bulk mole fractions X_{Ce} and X_{Mn} (main-text Fig. 4). Because both values use the same Γ-relaxed geometries, this difference isolates the k-sampling contribution at fixed geometry. Any additional geometry-response contribution, from re-relaxing each cell at the denser mesh, is expected to be smaller still: geometry optimization is variational, so each cell's response is second order in its small mesh-induced displacements, and the two responses partially cancel in E_{v} as the fixed-geometry errors do.

This shift exceeds the 14 meV pristine-cell error, so the k-sampling errors of the defective and pristine cells do not fully cancel: the defective cell carries the larger error (77 meV per supercell). The 62 meV residual is nonetheless small relative to the within-composition site-resolved spread (standard deviation 0.53 eV) and the inter-composition spread in E_{v} (0.1–1.0 eV), and it does not move this environment out of the 3.4–3.9 eV target window. Because the residual is well below the variations examined in the analysis, Γ-only production sampling does not change the reported trends.

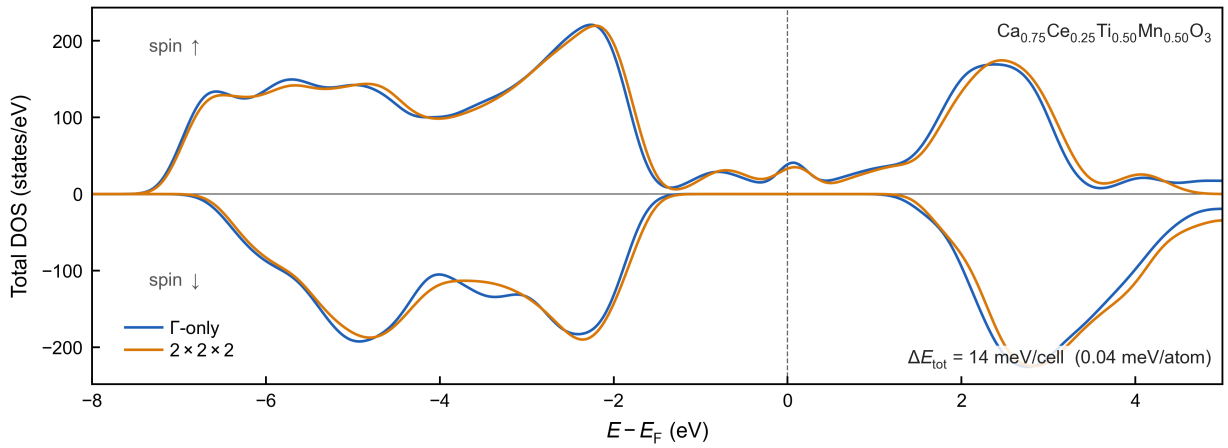


Figure S11: Spin-resolved total density of states for $Ca_{0.75}Ce_{0.25}Ti_{0.50}Mn_{0.50}O_3$ at Γ-only (blue) and at a Γ-centered $2 \times 2 \times 2$ Monkhorst–Pack mesh (orange), both evaluated as single-point self-consistent calculations on the same Γ-relaxed geometry. The dashed vertical line marks the Fermi level.

S11 Atomic properties used in CFM descriptors

The descriptors $\langle E_b \rangle$ and $\langle V_r \rangle$ in eqn (S1) are computed at each oxygen vacancy site as unweighted averages over the six first-nearest-neighbor cations of the vacant oxygen, comprising four A-site cations and two B-site cations:

$$\langle E_b \rangle = \frac{1}{6}\sum_{n=1}^{6} E_{b,n}, \quad \langle V_r \rangle = \frac{1}{6}\sum_{n=1}^{6} V_{r,n}. \tag{S20}$$

The per-cation crystal bond dissociation energy $E_{b,n}$ is the cohesive energy of the ground-state polymorph of the binary oxide of cation n in its assigned oxidation state, divided by the number of O^{2-}–cation bonds per formula unit[6]. The per-cation crystal reduction potential $V_{r,n}$ (in V relative to 1/4 mol of O_2(g)) is derived from the reduction energy of the binary oxide containing cation n to the binary oxide containing cation n in its next-lower oxidation state (ref. 6). This formulation modifies the original perovskite CFM of ref. 6, which used a sum over all six bonds for $\langle E_b \rangle$ and the maximum of the per-cation values among the nearest neighbors for $\langle V_r \rangle$, by replacing both with arithmetic means over the six neighbors; the change makes both descriptors site-resolved within the disordered SQS supercell and sensitive to the local cation environment at each symmetry-distinct oxygen site.

Tables S6 and S7 list the per-cation $E_{b,n}$ and $V_{r,n}$ values used in the two parameterizations of the parity comparison in Fig. S3. Both columns of each table are taken from ref. 6: the SCAN+U columns from their SCAN+U binary-oxide calculations, the experimental columns from their compilation of binary-oxide thermochemistry (their Fig. 4 and 5, and ref. 107–111 therein). The A-site cations and Ti are assigned fixed oxidation states (Ca^{2+}, Ce^{3+}, Ti^{4+}), whereas Mn is assigned a composition-dependent fractional valence $n_{Mn} = 4 - X_{Ce}/X_{Mn}$ (3.43–3.56 across the six compositions) when selecting $E_{b,n}$ and $V_{r,n}$; its descriptor values are obtained by linearly interpolating the Mn^{3+} and Mn^{4+} binary-oxide references (weights $4 - n_{Mn}$ and $n_{Mn} - 3$, respectively). These assignments serve only to select the binary-oxide reference values and do not otherwise reflect the local electronic state inferred from the SCAN+U calculations.

Table S6: Per-cation crystal bond dissociation energies $E_{b,n}$ used in the $\langle E_b \rangle$ descriptor, following ref. 6, eqn (2). Both columns are taken from the same work: the SCAN+U column from their SCAN+U binary-oxide calculations, the experimental column from their compilation of binary-oxide thermochemistry. The Mn^{4+} (MnO_2) and Mn^{3+} (Mn_2O_3) rows are the endpoints of the fractional-Mn interpolation described above.

			$E_{b,n}$ (eV)	
Cation	Oxidation state	Reference oxide	SCAN+U	Experimental
Ca	+2	CaO	1.88	1.83
Ce	+3	Ce_2O_3	2.48	2.52
Ti	+4	TiO_2	3.16	3.30
Mn	+4	MnO_2	2.25	2.25
Mn	+3	Mn_2O_3	1.97	1.96

Table S7: Per-cation crystal reduction potentials $V_{r,n}$ used in the $\langle V_r \rangle$ descriptor, given for the reduction of the assigned cation to its next-lower stable oxidation state. Following ref. 6 (eqn (5)), values are normalized per electron transferred and expressed relative to 1/4 mol of O_2(g). Both columns are taken from the same work: the SCAN+U column from their SCAN+U binary-oxide calculations, the experimental column from their compilation of binary-oxide thermochemistry. The $Mn^{4+} \longrightarrow Mn^{3+}$ and $Mn^{3+} \longrightarrow Mn^{2+}$ rows are the endpoints of the fractional-Mn interpolation described above.

	$V_{r,n}$ (V vs. O_2)	
Reduction	SCAN+U	Experimental
$Ca^{2+} \longrightarrow Ca^{0}$	−3.28	−3.29
$Ce^{3+} \longrightarrow Ce^{0}$	−2.95	−3.11
$Ti^{4+} \longrightarrow Ti^{3+}$	−1.91	−1.90
$Mn^{4+} \longrightarrow Mn^{3+}$	−0.40	−0.43
$Mn^{3+} \longrightarrow Mn^{2+}$	−1.02	−0.98

References

[1] R. B. Wexler, G. Sai Gautam, R. T. Bell, S. Shulda, N. A. Strange, J. A. Trindell, J. D. Sugar, E. Nygren, S. Sainio, A. H. McDaniel, D. Ginley, E. A. Carter and E. B. Stechel, *Energy & Environmental Science*, 2023, **16**, 2550–2560.

[2] B. Xu, J. Park, D. Zhang, H. A. De Santiago, W. Li, X. Liu, J. Luo, S. Lany and Y. Qi, *Chemistry of Materials*, 2024, **36**, 4990–5001.

[3] G. Sai Gautam and E. A. Carter, *Physical Review Materials*, 2018, **2**, 095401.

[4] G. Henkelman, A. Arnaldsson and H. Jónsson, *Computational Materials Science*, 2006, **36**, 354–360.

[5] W. Tang, E. Sanville and G. Henkelman, *Journal of Physics: Condensed Matter*, 2009, **21**, 084204.

[6] R. B. Wexler, G. S. Gautam, E. B. Stechel and E. A. Carter, *Journal of the American Chemical Society*, 2021, **143**, 13212–13227.

[7] M. D. Witman and P. Schindler, *Digital Discovery*, 2025, **4**, 625–635.

[8] F. Pedregosa, G. Varoquaux, A. Gramfort, V. Michel, B. Thirion, O. Grisel, M. Blondel, P. Prettenhofer, R. Weiss, V. Dubourg, J. Vanderplas, A. Passos, D. Cournapeau, M. Brucher, M. Perrot and É. Duchesnay, *J. Mach. Learn. Res.*, 2011, **12**, 2825–2830.

[9] S. P. Ong, W. D. Richards, A. Jain, G. Hautier, M. Kocher, S. Cholia, D. Gunter, V. L. Chevrier, K. A. Persson and G. Ceder, *Computational Materials Science*, 2013, **68**, 314–319.

[10] B. Baldassarri, J. He and C. Wolverton, *Physical Review Materials*, 2024, **8**, 055407.

[11] S. Lany, *Journal of the American Chemical Society*, 2024, jacs.4c02688.

[12] J. Park, B. Xu, J. Pan, D. Zhang, S. Lany, X. Liu, J. Luo and Y. Qi, *npj Computational Materials*, 2023, **9**, 29.

[13] *NIST Chemistry WebBook, NIST Standard Reference Database Number 69*, 2025, `https://webbook.nist.gov/chemistry/`, Online; accessed 2025.

[14] J. Chase, Malcolm W., *NIST-JANAF Thermochemical Tables*, American Institute of Physics, Woodbury, NY, 4th edn, 1998.

[15] M. D. Witman, A. Goyal, T. Ogitsu, A. H. McDaniel and S. Lany, *Nature Computational Science*, 2023, **3**, 675–686.

[16] T. Xie and J. C. Grossman, *Physical Review Letters*, 2018, **120**, 145301.

[17] T. C. Douglas, M. J. Dzara, A. J. E. Rowberg, K. A. King, M. Syrigou, N. A. Strange, R. T. Bell, A. Goyal, P.-W. Guan, R. B. Wexler, J. B. Varley, T. Ogitsu, S. Lany, A. H. McDaniel, S. R. Bishop and M. D. Witman, *Materials Horizons*, 2026, **13**, 829–839.

[18] M. D. Witman, S. Pujet, A. J. E. Rowberg, C. Sutton, J. B. Varley, S. Lany and R. B. Wexler, *Transfer learning on universal interatomic potential embeddings improves generalization in structure-property defect models*, 2026, `https://doi.org/10.26434/chemrxiv.15003938/v1`, Preprint.